

Effect of temperature on gamma radiation shielding capabilities of bauxite-based refractory concrete

Dominika Madej^{a,*}, Palina Cherkes^b, Michał Silarski^b

^a AGH University of Kraków, Faculty of Materials Science and Ceramics, Department of Ceramics and Refractories, Al. A. Mickiewicza 30, 30-059, Kraków, Poland

^b Jagiellonian University, Faculty of Physics, Astronomy and Applied Computer Science, Ul. Prof. Stanisława Łojasiewicza 11, 30-348, Kraków, Poland

ARTICLE INFO

Keywords:

Refractory concrete
Ba-,Fe-modified cements
Gamma radiation shielding capabilities
Microstructure
Ceramics

ABSTRACT

This work presents experimental and theoretical studies on gamma-ray shielding capabilities of bauxite-containing refractory concretes containing new types of inorganic cements belonging to the CaO-Al₂O₃ (as a reference), CaO-BaO-Al₂O₃-ZrO₂ and CaO-Al₂O₃-Fe₂O₃-ZrO₂ systems. Firstly, the structure, microstructure, hydration behavior of cements, and thermal stability analysis of hydration products were investigated using X-ray diffraction, scanning electron microscopy/energy-dispersive X-ray spectrometry (SEM-EDS) and Thermogravimetry-Differential Scanning Calorimetry (TG-DSC) coupled with Evolved gas analysis-mass spectrometry (EGA-MS). When both Fe₂O₃ and BaO occur in the form of hydraulic phases as Ca₂AlFeO₅ and BaAl₂O₄, respectively, or are structurally incorporated into Ca₇ZrAl₆O₁₈, the iron and barium modify the nature of hydration products of the CaO-Al₂O₃-H₂O-type. Secondly, three types of concretes containing refractory bauxite aggregates were developed and tested in terms of microstructure, phase content, volumetric density, and weight loss. The maximum weight loss at 110 °C was associated mainly with the evaporation of the capillary water and the physically adsorbed water (gel water), whereas the chemically bound water (crystal water) occurring in hydrates was released at higher temperatures. Slight variations of the volumetric density of the concretes due to temperature were found. The CCS of the concretes fell within the standard values of ca. 50–100 MPa for shielding refractory concretes. Finally, the effect of temperature on the gamma radiation shielding capabilities of concretes was evaluated using the transmission method for gamma rays with energy in the range of about 81–1400 keV. The obtained values of the linear and mass attenuation coefficients showed improvement in the shielding properties as compared with ordinary concrete. Moreover, the obtained results show no significant effect of elevated temperature on the gamma radiation attenuation properties of the studied bauxite-based refractory concretes which suggests that they may be very useful as shielding materials in severe thermal working conditions.

1. Introduction

Radiation shielding is an important issue when dealing with radioactive sources from equipment used in the nuclear fuels in nuclear power plants emitting ionizing radiation [1–5]. Ionizing radiation such as X-ray and gamma are harmful due to causing DNA damage, cell mutation, radiation illness, and finally cancer [6,7]. Thus, effective shielding is required to avoid radiation hazards. Gamma and X-rays are best absorbed by dense materials made of various heavy metals such as lead, nickel, chromium, bismuth, barium, iron, and tungsten [8–13]. The density of the composites with varying percentages of these components is one of the key factors influencing gamma ray attenuation

capabilities. Moreover, many oxides-based materials containing barium oxides, lead oxides, bismuth oxides, cadmium oxides, iron oxides, or a combination of thereof have been discussed in many papers for the shielding of nuclear radiations [14–19]. In this regard, many researchers have studied and reported various glass systems as promising gamma-ray shielding materials. They have also been added to concrete networks [17,20,21]. Because barium ions can protect against various forms of radiation, integrating them into the Portland clinker system of calcium aluminate cement-based clinker can yield a binder with shielding capabilities.

The lightweight, chemically stable, flexible, cost-effective, and free of toxic elements of alternatives to lead-based materials are in growing

* Corresponding author.

E-mail address: dmadej@agh.edu.pl (D. Madej).

<https://doi.org/10.1016/j.cemconcomp.2024.105608>

Received 29 March 2024; Received in revised form 14 May 2024; Accepted 25 May 2024

Available online 28 May 2024

0958-9465/© 2024 Elsevier Ltd. All rights are reserved, including those for text and data mining, AI training, and similar technologies.

demand as radiation shielding materials. Lead-containing shielding materials are of increasing concern because of the potential human health risks and the potential long-term harm to the environment caused by lead [22]. Lead can be replaced in many products by more sustainable and environment-friendly nontoxic and cost-effective elements, such as barium and iron-bearing compounds. Recently, a review paper dealing with the addition of barium compounds to radiation-shielding concrete was released by Seenappa et al. [23]. Barium-bearing compounds are the most common and favored radiation shielding materials because of their high shielding efficacy [24]. Barium sulfate (BaSO_4), barium tungstate (BaWO_4), barium chloride (BaCl_2), barium carbonate (BaCO_3), barium nitrate ($\text{Ba}(\text{NO}_3)_2$), barium fluoride (BaF_2) and barium chromate (BaCrO_4) is one of the most important groups of materials among barium compounds with the importance of the effective radiation shielding [9, 23, 25–27]. There are also many compounds in the Fe-bearing compounds family, among which hematite ($\alpha\text{-Fe}_2\text{O}_3$) and magnetite (Fe_3O_4) play an important role in the X-ray and gamma radiation shielding capabilities since the shielding effectiveness of composites was found to increase by incorporating iron-bearing components [28–32].

Due to low cost, ease of installation, mechanical properties, high versatility, high durability, and effectiveness concrete can be implemented as an effective shielding material against ionizing radiation, as evident from the many works on the topic [1, 33–35]. The current main technical approach to designing radiation shielding concretes uses special aggregates of high specific gravity as fillers, cement, additives, and water. Aggregates are the major constituents of concrete and they generally occupy 70–80 % of the volume of concrete, and can therefore be expected to have an important influence on their shielding properties [36]. Consequently, works on heavy concrete for radiation shielding have mostly focused on heavy aggregates [37–40]. There are two types of aggregate used for this purpose, first the natural mineral aggregates of either high density or high crystalline water content, or both, and second the synthetic aggregates. The first group includes materials such as barite, magnetite, hematite, ilmenite, and serpentine [30, 39–52]. Synthetic aggregates include iron and steel slags, ferrophosphorus, boron frit, boron carbide, calcium carbide, and alkali-activated slag composites incorporating cement clinker aggregates [53–61]. Different types of cement including Ordinary Portland Cement (OPC), calcium silicate cement, calcium aluminate cement (CAC), barium silicate cement, strontium silicate cement, high magnesia Portland cement, boron-containing cement, gypsum aluminate cement, boron and iron-containing phosphate cement, and special refractory cement [20, 62, 63] are proposed. Recent research endeavors in OPC production have pivoted towards mitigating its environmental footprint. The promising alternatives explored in these efforts are aluminates-based cements, which offer distinct advantages in terms of structural purity and cost-effectiveness compared to traditional OPC.

Many hydration products (hydrates) are formed in the reaction of cement with water. These components increase the amount of crystallized water in radiation-shielding concrete, which is beneficial for neutron attenuation. Cements containing barium and iron can protect against both neutrons and γ -rays due to their higher effective atomic numbers. Since, hydrates continuously undergo phase changes as temperature increases, both concrete properties such as strength, modulus of elasticity, and volumetric deformation, and the structural quality of concrete are significantly deteriorated [64–66]. It is commonly known that concrete may be exposed to elevated temperatures during a fire when the heat is transferred from the hot part of the reactor system or due to the energy deposited by radiation emerging in the reactor core (mainly gamma rays and neutrons). The reactor shield may be exposed to temperatures even higher than 500 °C for a long time. Thus, an increase in porosity due to the release of chemically bound water, a decrease in mechanical strength due to concrete matrix decomposition, growth of cracks, and even spalling will occur in concrete which will affect both the radiation shielding performance and the safety and durability of the building. Numerous studies have been carried out on

the effects of elevated temperatures on the properties of different types of radiation-shielding concrete. Luo et al. [65] evaluated both the mechanical and γ -ray shielding properties and acoustic emission characteristics of barite- and magnetite-based concrete exposed to elevated temperatures. Sancak et al. [67] gave comparison research on the effects of elevated temperature on compressive strength and weight loss of the lightweight concretes and concretes with normal-weight aggregate. Ali et al. [43] investigated the physical, mechanical, and microstructural properties of magnetite heavyweight concrete and compared it with quartz concrete after exposure to elevated temperatures.

Considering studies conducted by other researchers so far, it becomes evident that no works have been conducted on the effect of high temperatures on the shielding properties of concretes containing refractory aggregates and refractory cements. Therefore, this work is focused on studying the effect of the temperatures of 25, 110, and 400 °C on the shielding properties of bauxite-based concretes containing CAC, Fe-/Ba-modified C-A-Z cements. The attenuation coefficients are measured in the γ -rays energy region of 81–1408 keV corresponding to the vast part of the γ -rays generated in the nuclear reactors. Radiation in this energy range is also used in laboratories in research and development and hospitals for therapy and diagnostics.

2. Experimental part

2.1. Synthesis of Fe- and Ba-modified C-A-Z cement clinkers

The powders of Fe- and Ba-modified C-A-Z cements were prepared via a classical ceramic method which used oxides (98.5 % ZrO_2 from Acros Organics, 99 % Al_2O_3 from Acros Organics, 97 % Fe_2O_3 from Sigma-Aldrich) and carbonates (99 % CaCO_3 from POCH, 99.9 % BaCO_3 from POCH) as described below. The starting materials in a suitable stoichiometry corresponding to $7\text{CaO}\cdot 2.5\text{Al}_2\text{O}_3\cdot 0.5\text{Fe}_2\text{O}_3\cdot \text{ZrO}_2$ (Fe-modified C-A-Z cement) and $6\text{CaO}\cdot \text{BaO}\cdot 3\text{Al}_2\text{O}_3\cdot \text{ZrO}_2$ (Ba-modified C-A-Z cement) were homogenized in a ball mill for a period of 2 h. The powders were uniaxially pressed at a pressure of 70–80 MPa to obtain green pellets and calcined at 1200 °C for 10 h. To increase the homogeneity distribution of the components, the second homogenization step of calcined samples was involved. The pellet samples were again prepared using a press at the same pressure and were then sintered at 1300 °C (Fe-modified sample) or 1400 °C (Ba-modified sample) for 20 h. Moreover, the detailed synthesis procedure of reference $\text{C}_7\text{A}_3\text{Z}$ cement is presented elsewhere [68–70].

The sinters of Fe-, Ba-modified C-A-Z cement clinkers were embedded in resin, ground, and polished using a 0.1 μm diamond paste to achieve a mirror-like surface finish. Microstructural features of the carbon-coated sample were examined by scanning electron microscopy (SEM, Nova Nano SEM 200 FEI) combined with energy-dispersive X-ray spectroscopy (EDS).

Then, the all sinters were crushed and milled to obtain fine powders below 63 μm . Phase identification was performed by the X-ray powder diffraction (XRD) method on a PANalytical Empyrean multifunction X-ray diffractometer. XRD measurements were made using a $\text{Cu-K}\alpha$ radiation tube between 5° and 45° in scattering angle 2 θ and step size of 0.02°. The phase composition was estimated by the X-Pert High Score Plus (PANalytical) software and the ICDD PDF-4 database.

Particle size distribution of cements was measured by a laser diffraction analyzer (the Master Sizer 2000 Ver. 5.60 apparatus of Malvern (UK)).

2.2. Cement-based pastes preparation and methods of investigations

Since the initial strength development of cement-bonded refractory concretes was mostly governed by cement hydration, the hydration process of the Fe- and Ba-modified C-A-Z cements were tracked by XRD, DSC-TG-EGA(MS), and SEM-EDS. The tests were conducted on cement pastes prepared with the use of as-synthesized cements and water. Based

Table 1
Batch compositions of concretes (wt.%).

Raw materials	Index	Concrete code		
		C-A	C-B	C-C
Calcined bauxite aggregate	0–3 mm	68.0	68.0	68.0
Calcined bauxite fume	<0.063 mm	10.0	10.0	10.0
Microsilica	971U	2.0	2.0	2.0
Reactive alumina	CTC40	10.0	10.0	10.0
Calcium aluminate cement (CAC)	Górkal 70	10.0	–	–
Ba-doped C-A-Z cement	–	–	10.0	–
Fe-doped C-A-Z cement	–	–	–	10.0
Dispersant	Castament®FS 20	0.1	0.1	0.1
Water	5.0	5.0	5.0	5.0

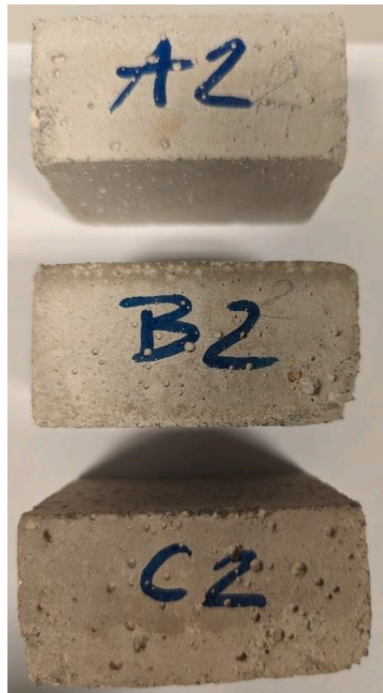


Fig. 1. Photos of prepared concrete samples.

on trial and error, a water-to-cement (w/c) ratio of 1.0 was selected to attain good consistency of the cement pastes. Two cement pastes were mixed by hand in a glass beaker for 5 min, then poured into sealed polyethylene bags and placed in a climatic chamber (at the temperature of 50 °C, relative humidity of ca. 95 %) to prevent loss of moisture and left to harden for 7 days. Moreover, two reference cement pastes containing CAC or $\text{Ca}_7\text{ZrAl}_6\text{O}_{18}$ were also cast to SEM and XRD investigations. At the required age of 15 min, 30 min, 1 h, 24 h, 3 days, and 7 days, the hardened cement pastes were grounded in an agate mortar and subjected to solvent exchange to stop any further hydration. For this purpose, cold acetone was used as a solvent. By coupling a Thermogravimetry (TG), and Differential Scanning Calorimetry (DSC) with a Quadrupole Mass Spectrometer (QMS), it was possible to evaluate the hydrated compounds and hydration degree. To identify the crystalline phases, the acetone-washed samples were analyzed by XRD. The fracture surfaces of hardened cement pastes were investigated by SEM-EDS.

2.3. Refractory concrete preparation and methods of investigations

Calcined bauxite aggregate ($\text{Al}_2\text{O}_3 \geq 88.5\%$), calcined bauxite fume ($\text{Al}_2\text{O}_3 \geq 88.5\%$), reactive alumina (Almatis CTC40), microsilica (Elkem 971U), binder, additive, and water were used as raw materials to prepare refractory concretes. Three different aluminate binders were used

for concrete materials preparation, i.e. calcium aluminate cement (CAC) Górkal 70 from Górkal Cement Sp. z o.o. in concrete A (as a reference), presynthesized Ba-containing C-A-Z cement in concrete B, and presynthesized Fe-containing C-A-Z cement in concrete C. The Dinger and Funk's particle sizing model was used to design the particle size distribution with the q value of 0.26 to achieve a balance between good compaction and rheology. Table 1 presents the details of the formulated refractory concretes with different types of aluminous cements. Each composition of concretes was selected in such a way that the conversion process of metastable hydrates into stable products was controlled and inhibited. In this context, it should be considered that microsilica, the dispersant's components, and both Ba and Fe ions have allowed stabilizing the structure of hydrates initially formed in the concrete samples. Thus, spalling phenomena, crack, and strength reduction versus storing time were not observed.

The fine components of the refractory concretes were mixed for 1 min. Then, the bauxite aggregate was added, and the combination was mixed for 3 min. Finally, a mixture of water and dispersant was added, and the combination was mixed for the next 5 min. The three kinds of concrete in Table 1 were poured into cube molds (Fig. 1). Two cubes ($\sim 50 \times 50 \times 50$ mm and $\sim 70 \times 70 \times 35$ mm) were cast from each batch, cured at a temperature of 50 °C for 24 h under a relative humidity of $\sim 95\%$ and finally heat-treated at 110 °C, 200 °C, and 400 °C. During the experiments, the drying time does not exceed 24h, while the dry-out process of cement-bonded castables involves two next stages ongoing for 2 h at 200 °C and 400 °C. The concrete volume densities (g/cm^3) were determined by dividing the mass of a sample by the volume occupied by that sample after each of the heat treatments.

The weight loss of concrete specimens exposed to high temperatures was calculated using Eq. (1) [66]:

$$\text{Loss of weight (\%), } \Delta W_f = \left(\frac{W_b - W_a}{W_b} \right) \times 100 \quad (1)$$

where:

- W_b : Weight before exposure of the specimen to each temperature, e. g. 200 °C
- W_a : Weight of the specimen after the thermal process, e.g. 400 °C
- ΔW_f : Weight loss percentage.

The cold crushing strength (CCS) of the concrete materials C-A, C-B, and C-C heat treated at 110, 200, and 400 °C were determined according to the PN EN 993-5 standard.

Microstructural characterization was performed to analyze the microstructural properties of refractory concretes with various cements, especially phase distribution by using SEM-EDS. Before the microstructural analysis, the samples were cut, embedded in resin, ground, and finally polished. Before observation, all samples were coated with carbon. To conduct XRD analysis, the concrete samples were manually ground into powder using a mortar and pestle.

2.4. Radiation shielding characterization of concretes

Investigation of the radiation attenuation properties of the studied materials was performed using the transmission method for γ -rays with energy in the range of about 120–1400 keV. We have used several isotopes emitting γ quanta with well-defined energies: ^{22}Na (511 and 1275 keV), ^{60}Co (1173 and 1333 keV), ^{137}Cs (662 keV), and ^{152}Eu (122, 245, 344, 779, 964, 1086, 1112, 1408 keV). Samples of the tested materials were placed between the radiation source and an ORTEC GMX25P4-70 High Purity Germanium detector (HPGe) measuring the energies of the transmitted γ -rays with a resolution much better than 1 % for the studied lines [20]. The detector was shielded from the laboratory background with a lead cylinder and read out by the TUKAN multichannel analyzer. Details of the experimental setup can be found in [20]. We have

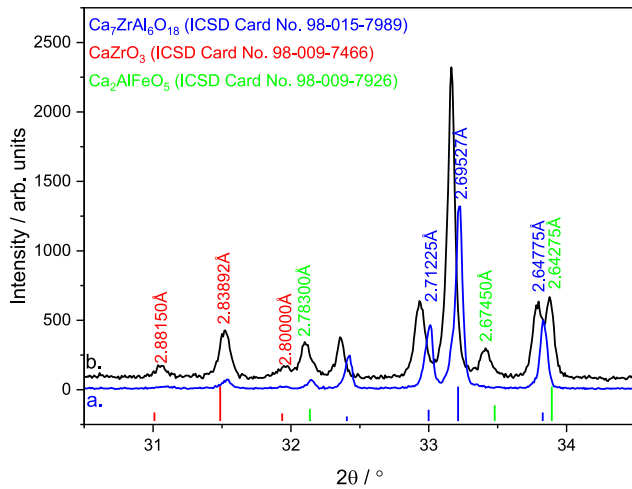


Fig. 2. X-ray diffraction patterns of reference calcium zirconium aluminate cement (a) and Fe-modified C-A-Z cement (b). The vertical bars indicate the reference peak positions of all phases identified.

determined the number of γ quanta transmitted through the sample by integrating maxima of full absorption for all the studied energies. This ensures that the counted number of photons corresponds solely to the radiation which did not interact with the material. All the peaks were integrated in a region corresponding to the $\pm 3\sigma$ (standard deviation) range around its maximum for all the measurements. We have used distributions of the determined numbers of the transmitted γ -rays with a given energy in a function of the thickness to characterize the studied material. As expected, the obtained data follow the exponential reduction of the radiation flux with increasing thickness of the absorber for all the radiation lines. Thus, fitting a model in the form of the exponential curve: $N(x) = N_0 e^{-\mu x}$ (or its logarithmic form) allowed us to estimate the linear attenuation coefficient μ . Here N_0 stands for the number of γ quanta registered with a bare source and detector (with no absorber installed in the setup), and $N(x)$ denotes the same quantity measures with an absorber of thickness x .

The measured linear attenuation coefficients allowed us to estimate the other useful quantities using additionally the known densities and elemental content. Thus, we have determined also the Half-Value Layer (the average amount of material needed to reduce the radiation intensity by 50 %):

$$l_{HVL} = \frac{\ln(2)}{\mu} \quad (2)$$

and the total atomic cross section [71]:

$$\sigma_a = \frac{\mu_m}{N_a \sum_i w_i / A_i} \quad (3)$$

where N_a denotes the Avogadro number, w_i is the proportion by weight of the material's i th constituent element and A_i stands for its atomic weight. The parameter μ_m is called the mass attenuation coefficient and is equal to $\mu_m = \frac{\mu}{\rho}$, where ρ stands for the density of the material.

3. Results

3.1. Phase analysis, microstructure characterization and particle size distribution of the presynthesized Fe- and Ba-modified C-A-Z cements

3.1.1. Fe-modified C-A-Z cement

X-ray diffraction experiment indicates that the reference undoped sample contains calcium zirconium aluminate as a major phase (Fig. 2a). The principal peaks are located at 2θ of 33.213° (d-spacing 2.69527 \AA), 32.999° (d-spacing 2.71225 \AA), and 33.827° (d-spacing 2.64775 \AA), according to the ICSD Card No. 98-015-7989. The reference sample shows the peaks of the secondary phase at ca. 31.487° (d-spacing 2.83892 \AA), 31.010° (d-spacing 2.88150 \AA) and 31.937° (d-spacing 2.80000 \AA) typical of CaZrO_3 , according to the ICSD Card No. 98-009-7466. Fig. 2b shows the room-temperature XRD pattern of Fe-modified C-A-Z cement. XRD study proves the three-phase character of this cement. The diffraction peaks of this sample were well matched with $\text{Ca}_7\text{ZrAl}_6\text{O}_{18}$ (ICSD Card No. 98-015-7989), CaZrO_3 (ICSD Card No. 98-

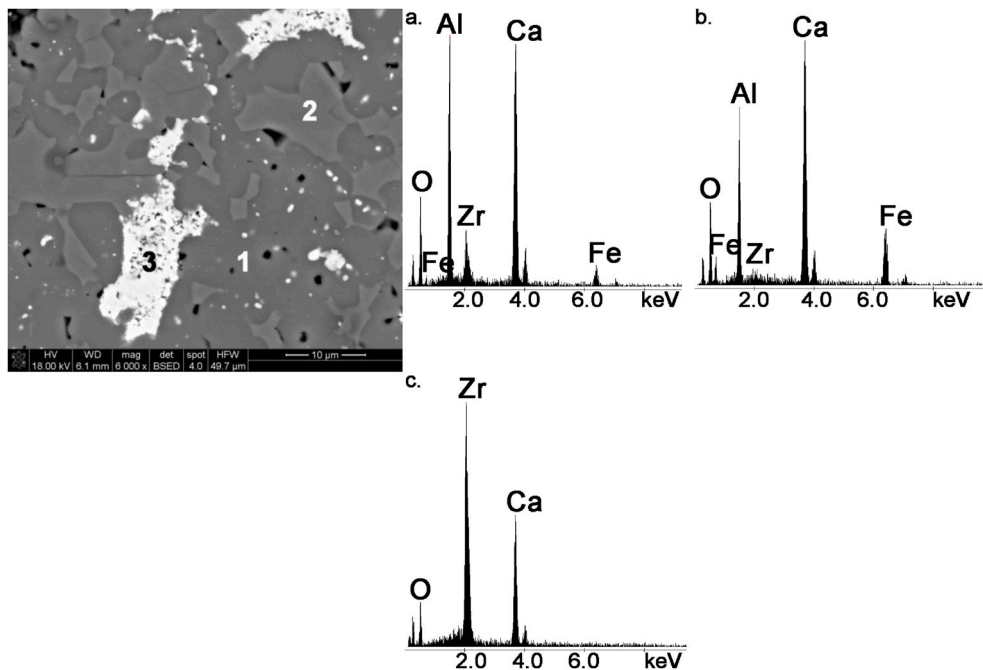


Fig. 3. SEM micrograph of Fe-modified C-A-Z clinker. EDS analysis in points 1 – Fe-doped $\text{Ca}_7\text{ZrAl}_6\text{O}_{18}$ (a.), 2 – $\text{Ca}_2\text{AlFeO}_5$ (b.), 3 – CaZrO_3 (c.).

Table 2

EDS analysis of phases present in the Fe-modified C-A-Z cement clinker given as an average of five points together with those of references.

Phase	Elements in wt. %				
	Ca	Al	Zr	Fe	O
Theoretical composition of reference $\text{Ca}_7\text{ZrAl}_6\text{O}_{18}$	34.17	19.65	11.11	–	35.07
Measured composition of $\text{Ca}_7\text{ZrAl}_6\text{O}_{18}$ in Fe-modified C-A-Z cement clinker	34.72	20.30	10.27	7.06	27.65
Theoretical composition of reference $\text{Ca}_2\text{AlFeO}_5$	33.02	11.07	–	22.97	32.94
Measured composition of $\text{Ca}_2\text{AlFeO}_5$ in Fe-modified C-A-Z cement clinker	33.07	14.17	1.93	23.04	27.79
Theoretical composition of reference CaZrO_3	22.36	–	50.86	–	26.77
Measured composition of CaZrO_3 in Fe-modified C-A-Z cement clinker	23.32	0.43	54.66	1.29	20.30

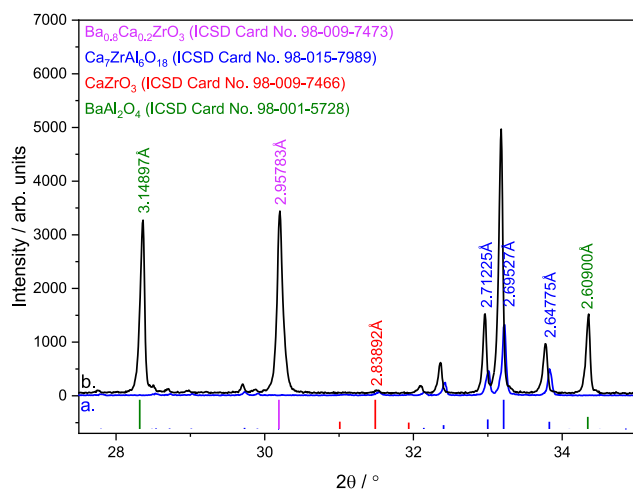


Fig. 4. X-ray diffraction patterns of reference calcium zirconium aluminate cement (a) and Ba-modified C-A-Z cement (b). The vertical bars indicate the reference peak positions of all phases identified.

009-7466) and $\text{Ca}_2\text{AlFeO}_5$ (ICSD Card No. 98-009-7926). These results also show that the Fe^{3+} dopant has successfully entered the $\text{Ca}_7\text{ZrAl}_6\text{O}_{18}$ and CaZrO_3 lattices and formed solid solutions. XRD data confirms peaks shifting to a lower 2θ value, which indicates an expansion to a higher lattice parameter. Moreover, the formation of tetracalcium aluminoferrite phase ($\text{Ca}_2\text{AlFeO}_5$ or C_4AF) was proved according to the characteristic Bragg peaks positioned at 33.893° (d-spacing 2.64275 Å), 33.478° (d-spacing 2.67450 Å) and 32.137° (d-spacing 2.78300 Å) according to the ICSD Card No. 98-009-7926.

The Fe-doped CAZ cement clinker sample showed a coarse-grained texture (Fig. 3). At a sintering temperature of 1300°C this sample had a close pore structure. This sintering temperature developed predominantly irregularly shaped pores up to ca. $1\text{--}3\ \mu\text{m}$ long, which appeared between the clinker phases. Densification of the microstructure led to an increase in connectivity between the phases, which resulted in a reduction in the number of open pores. Microstructure analysis with qualitative phase identification using SEM-EDS is in very good accordance with the results of XRD analysis, which showed that the targeted phase composition was reached in this clinker composition. The main constituent was calcium zirconium aluminate (Fig. 3a-point 1), evident by the presence of the continuous phase acting as a matrix to hold other inclusions. In places the tetracalcium aluminoferrite phase grains (Fig. 3b-point 2) were connected by their necks or were grains dispersed

in the matrix phase. Concerning the minor phase, grains of calcium zirconate (Fig. 3c-point 3) were agglomerated to form a particle of about $5\text{--}20\ \mu\text{m}$ in length that appeared between the grains of calcium zirconium aluminate and tetracalcium aluminoferrite. The EDS analysis has proved that the all phases identified were elaborated with good stoichiometry corresponding to the $\text{Ca}_7\text{ZrAl}_6\text{O}_{18}$, CaZrO_3 , and $\text{Ca}_2\text{AlFeO}_5$. Table 2 shows the results of weight percentages of the elements contained in the three regions under study of the Fe-doped C-A-Z clinker obtained by EDS analysis. From the results presented in Table 2, it can be seen that the element-weight percentages of the micro areas of each grain determined by quantitative EDS microanalysis in SEM are in very good agreement with the weight concentration of elements in stoichiometric compounds. Moreover, EDS analysis has confirmed the incorporation of Fe dopant in both $\text{Ca}_7\text{ZrAl}_6\text{O}_{18}$ and CaZrO_3 .

3.1.2. Ba-modified C-A-Z cement

Fig. 4 presents the XRD patterns of Ba-modified C-A-Z cement clinker, synthesized by the reaction-sintering process for preparing cement clinker. The XRD pattern of the undoped $\text{Ca}_7\text{ZrAl}_6\text{O}_{18}$ cement clinker from Ref. [72] has been also added for comparison. The major phases in the Ba-modified C-A-Z cement are clearly $\text{Ca}_7\text{ZrAl}_6\text{O}_{18}$ (ICSD Card No. 98-015-7989), BaAl_2O_4 (ICSD Card No. 98-001-5728) and $\text{Ba}_{0.8}\text{Ca}_{0.2}\text{ZrO}_3$ (ICSD Card No. 98-009-7473). Secondary phase CaZrO_3 (ICSD Card No. 98-009-7466) is also identified in both Ba-modified C-A-Z cement clinker and reference material [73,74]. Since the sample contains Ba, the peaks of $\text{Ca}_7\text{ZrAl}_6\text{O}_{18}$ are subtly shifted to a lower angle and become broader slightly. This effect is especially noticeable for the most intense Bragg peaks that are originally located at 2θ of 33.213° (d-spacing 2.69527 Å), 32.999° (d-spacing 2.71225 Å), and 33.827° (d-spacing 2.64775 Å) (Fig. 4a). The origin behind these changes is the incorporation of the larger Ba atoms in the $\text{Ca}_7\text{ZrAl}_6\text{O}_{18}$ matrix. The substitution of Ca ions (194 p.m.) with Ba (253 p.m.) leads to the enlargement of the unit cell of the $\text{Ca}_7\text{ZrAl}_6\text{O}_{18}$. Similar observations have been reported for the substitution of Ca ions (194 p.m.) with Sr (219 p.m.) [75,76]. The formation of barium mono-aluminate (BaAl_2O_4) was verified based on the characteristic peaks at 2θ of 28.319° (d-spacing 3.14897 Å) and 34.345° (d-spacing 2.60900 Å) as confirmed by a standard card file No. 98-001-5728, whereas typical peak for barium calcium zirconate is visible at 2θ of 30.191° (d-spacing 2.95783 Å, ICSD Card No. 98-009-7473). In addition, at the 2θ value of nearly 31.487° (d-spacing 2.83892 Å), the low-intensity peak of the calcium zirconate (ICSD Card No. 98-009-7466) phase can also be observed.

SEM image of the polished surface of the Ba-modified C-A-Z cement clinker is shown in Fig. 5. A dense and uniform microstructure (large grain size above $10\ \mu\text{m}$; small grain size below $10\ \mu\text{m}$; very small inclusions within the grains below $1\ \mu\text{m}$) was clearly visible in the sample, as shown in Fig. 5. This triple microstructure significantly improves the densification of the Ba-modified C-A-Z cement clinker. SEM-EDS analysis of this sample confirmed the formation of the target phases of calcium zirconium aluminate, barium mono-aluminate, and barium calcium zirconate, as indicated by the XRD results. Three distinct regions, dark grey, light grey, and white, can be observed from the microstructure of the Ba-modified C-A-Z cement clinker sample. The EDS analysis of the sample showed that the dark grey region was concentrated with Ca, Ba, Al, Zr, and O, which corresponds to the Ba-doped $\text{Ca}_7\text{ZrAl}_6\text{O}_{18}$ (Fig. 5a, point 1), as proved by the XRD pattern. The light grey phase was rich with Ba, Al, and O, which corresponds to the BaAl_2O_4 (Fig. 5b, point 2), as proved by XRD. The white phase was identified as $(\text{Ba,Ca})\text{ZrO}_3$ (Fig. 5c, point 3) phase by XRD. Table 3 presents the results of weight percentages of the elements contained in the three regions of the Ba-doped C-A-Z clinker obtained by the EDS analysis together with the calculated theoretical weight concentration of elements in stoichiometric compounds. SEM-EDS results are presented showing good agreement when compared to both calculated concentrations of elements and XRD phase identification. Furthermore, the EDS analysis confirms the existence of Ba-rich particles of $\text{Ca}_7\text{ZrAl}_6\text{O}_{18}$ (dark

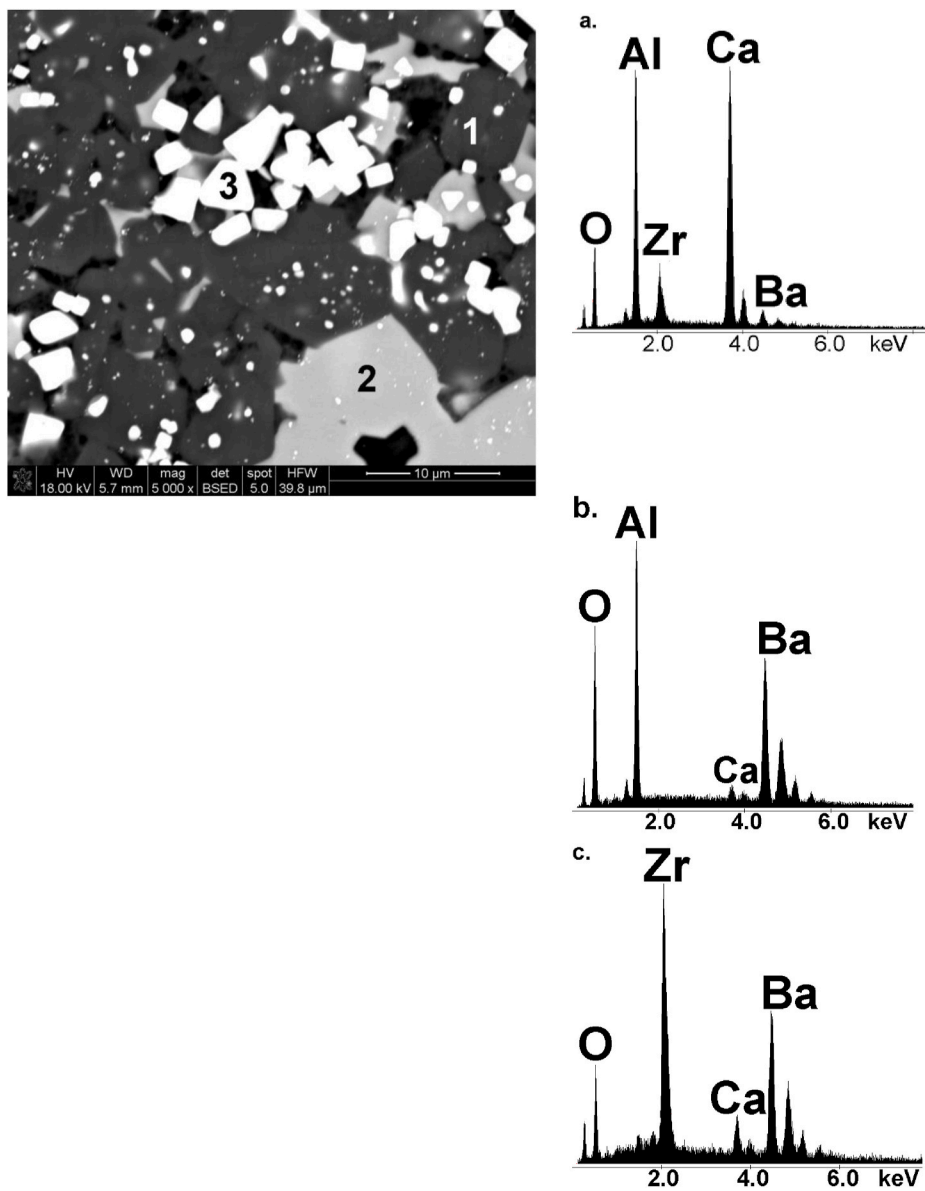


Fig. 5. SEM micrograph of Ba-modified C-A-Z clinker. EDS analysis in points 1 – Ba-doped $\text{Ca}_7\text{ZrAl}_6\text{O}_{18}$ (a.), 2 – BaAl_2O_4 (b.), 3 – $(\text{Ba,Ca})\text{ZrO}_3$ (c.).

Table 3

EDS analysis of phases present in the Ba-modified C-A-Z cement clinker given as an average of five points together with those of references.

Phase	Elements in wt. %				
	Ca	Al	Zr	Ba	O
Theoretical composition of reference $\text{Ca}_7\text{ZrAl}_6\text{O}_{18}$	34.17	19.65	11.11	–	35.07
Measured composition of $\text{Ca}_7\text{ZrAl}_6\text{O}_{18}$ in Ba-modified C-A-Z cement clinker	35.56	20.22	10.72	9.41	24.09
Theoretical composition of reference BaAl_2O_4	–	21.09	–	53.82	25.09
Measured composition of BaAl_2O_4 in Ba-modified C-A-Z cement clinker	1.42	23.23	0.17	60.05	15.13
Theoretical composition of reference BaZrO_3	–	–	32.98	49.66	17.36
Measured composition of BaZrO_3 s. s. in Ba-modified C-A-Z cement clinker	3.15	1.04	34.68	50.60	10.53

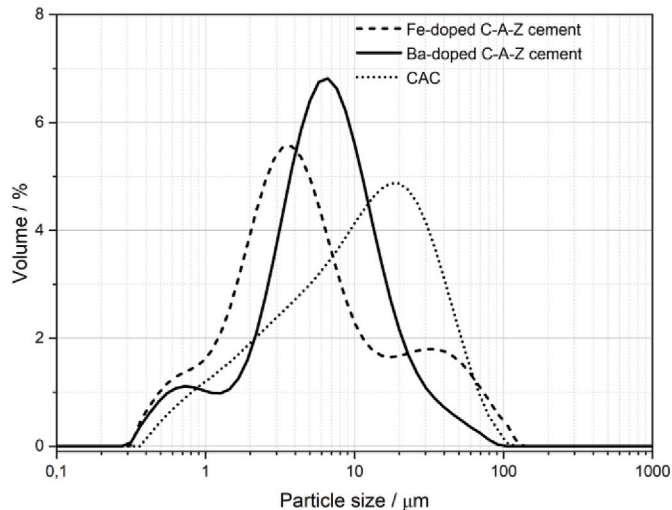


Fig. 6. Particle size distribution of cements.

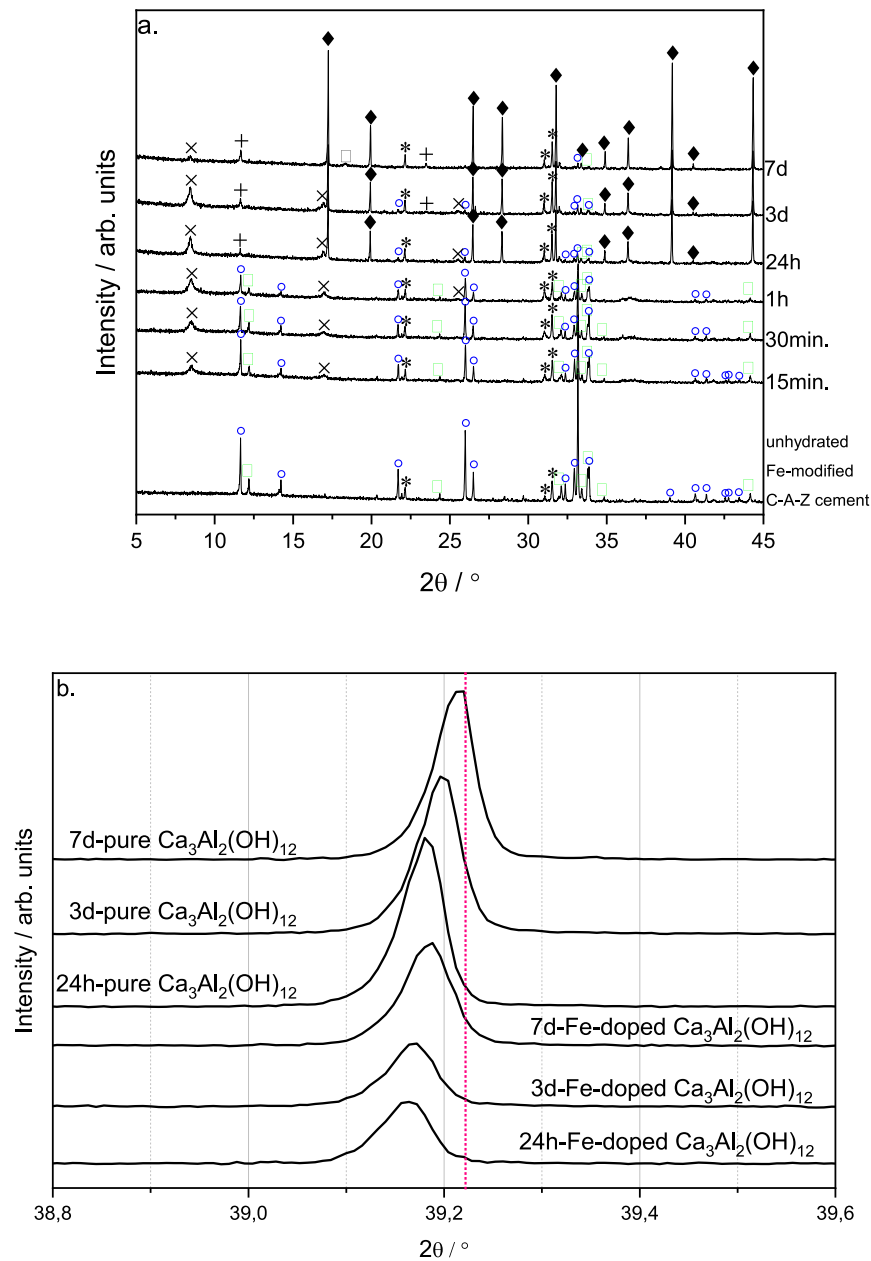


Fig. 7. X-ray diffraction patterns of Fe-modified C-A-Z cement when hydrated between 15 min and 7 days (a). Cement paste prepared with $w/c = 1.0$ cured at 50°C . The markers indicate the reference peak positions of reference data for all phases identified: \circ $\text{Ca}_7\text{ZrAl}_6\text{O}_{18}$ (ICSD Card No. 98-015-7989), \ast CaZrO_3 (ICSD Card No. 98-009-7466), \circ $\text{Ca}_2\text{AlFeO}_5$ (ICSD Card No. 98-009-7926), \blacklozenge $\text{Ca}_3\text{Al}_2(\text{OH})_{12}$ (ICDD Card No. 00-024-0217), \times $3\text{CaO}\cdot\text{Al}_2\text{O}_3\cdot\text{Ca}(\text{OH})_2\cdot 18\text{H}_2\text{O}$ (ICDD Card No. 00-042-0487)/ $\text{Ca}_2\text{Al}_2\text{O}_5\cdot 8\text{H}_2\text{O}$ (ICDD Card No. 00-045-0564), $+$ $\text{C}_3\text{A}\cdot\text{CaCO}_3\cdot 11\text{H}_2\text{O}$ (ICDD Card No. 00-036-0377), ∇ $\text{Al}(\text{OH})_3$ (ICSD Card No. 98-003-6233). Position 2θ of the "100 % peak" of undoped $\text{Ca}_3\text{Al}_2(\text{OH})_{12}$ according to the ICDD Card No. 00-024-0217 marked as a pink vertical line (b). The undoped $\text{Ca}_3\text{Al}_2(\text{OH})_{12}$ was synthesized through the $\text{Ca}_7\text{ZrAl}_6\text{O}_{18}$ hydration.

grey regions, Fig. 5a, point 1) and this is in good agreement with the XRD analysis that a homogeneous solid solution was formed.

3.1.3. Particle size distribution

After sintering, the Fe-doped and Ba-doped C-A-Z and C-Sr-A-Z clinkers were ground to a median particle size ($d_{0.5}$) of ca. $4.6\ \mu\text{m}$ and ca. $6.6\ \mu\text{m}$, respectively (Fig. 6). As a reference commercially available CAC was also presented with the $d_{0.5}$ value of ca. $12.0\ \mu\text{m}$. The as-synthesized cements reveal a broad bimodal particle size distribution. By comparison, the respective particle size distribution of the CAC sample was

monomodal.

3.2. Tracking in the hydration process of Fe- and Ba-modified C-A-Z cements via XRD, DSC-TG-EGA(MS) and SEM-EDS

3.2.1. Fe-modified C-A-Z cement

The paste made with the Fe-modified C-A-Z cement was analyzed using X-ray diffraction, DSC-TG-EGA(MS), and SEM-EDS up to 7 days of hydration. As shown in Fig. 7, the main hydration products obtained from the hydration of neat Fe-modified C-A-Z cement-based cement

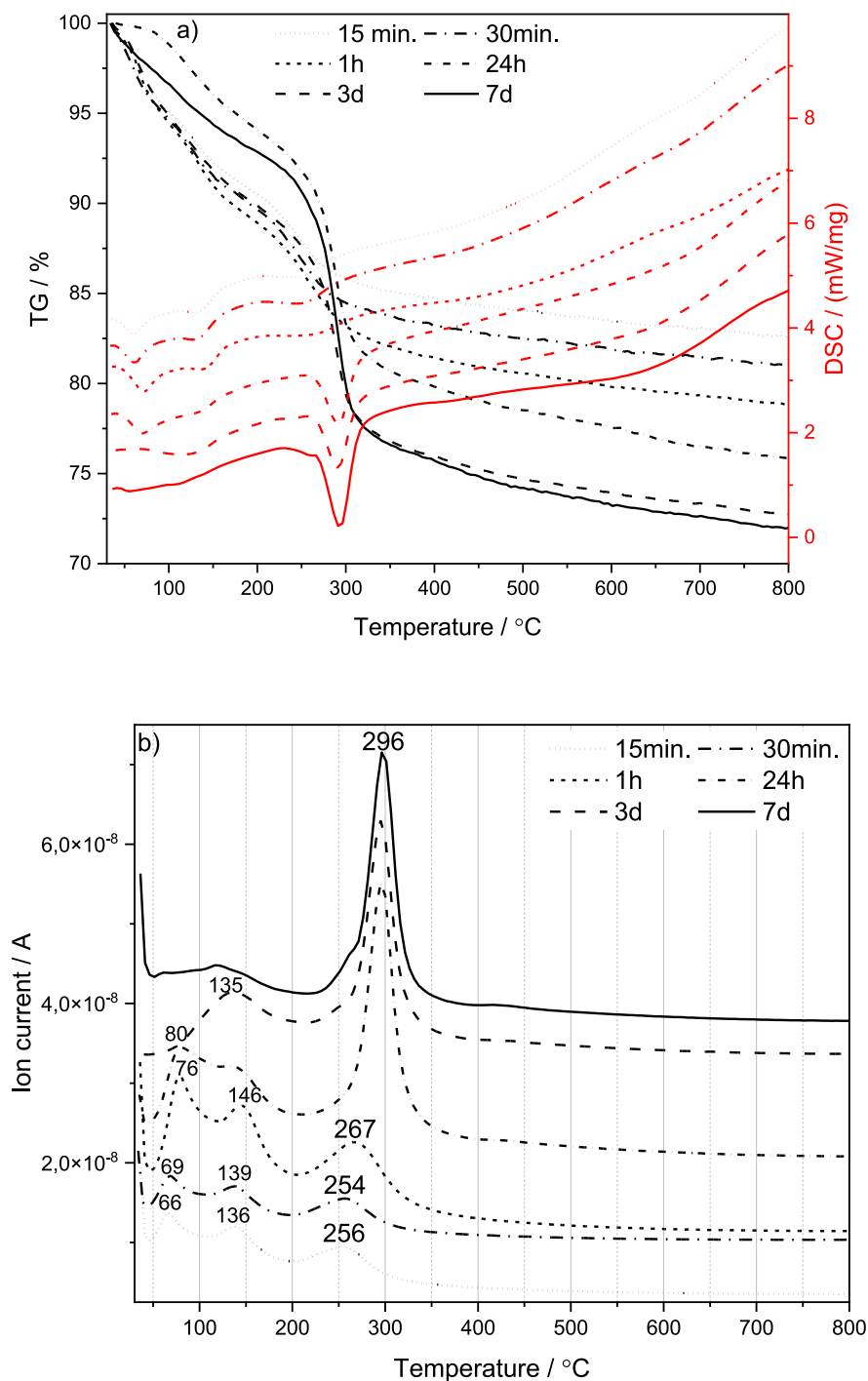


Fig. 8. The TG and DSC curves summarizing the thermal behavior of the Fe-modified C-A-Z cement paste when heated from 30 to 800 °C at 10 °C/min (a). Gas evolution curves for representative mass spectroscopic ion fragment of H₂O⁺ (*m/z* = 18) vapors during the thermal decomposition of the Fe-modified C-A-Z cement paste (b). Cement paste prepared with *w/c* = 1.0 cured at 50 °C. Hydration at ages 15 min to 7 days.

paste are two metastable hexagonal phases C₄AH₁₉ or C₂AH₈ at first minutes and an hour of reaction. The diffraction peaks belonging to C₄AH₁₉ coincide with those of C₂AH₈, suggesting that both hydrates were formed. Hence, a clear distinction between these two hydration products is difficult at this stage. The 100 % main diffraction peak corresponding to the C₄AH₁₉ or C₂AH₈ hydrates appears at 2θ of 10.64350° (d-spacing 8.301 Å) and 10.81270° (d-spacing 8.170 Å) which are in very good agreement with ICDD Card No. 00-042-0487 and ICSD Card No. 00-045-0564 for C₄AH₁₉ and C₂AH₈, respectively. By the

presence of iron, the hydration is prolonged even up to 7 days, as evident from the presence of the peak characteristics for unhydrated parts of Fe-doped C₇A₃Z and C₄AF grains (Fig. 7a). Analysis of the XRD results showed that the presence of iron strongly reduced the rate of reactions, which was also related to inhibition of the conversion reaction. Generally, the hydrates C₄AH₁₉ and C₂AH₈ are both metastable phases that transform, or convert, with time or due to temperature to the more stable C₃AH₆ [77]. The formation of a thermodynamically stable product of cement hydration, i.e. C₃AH₆, is strongly evident by the presence

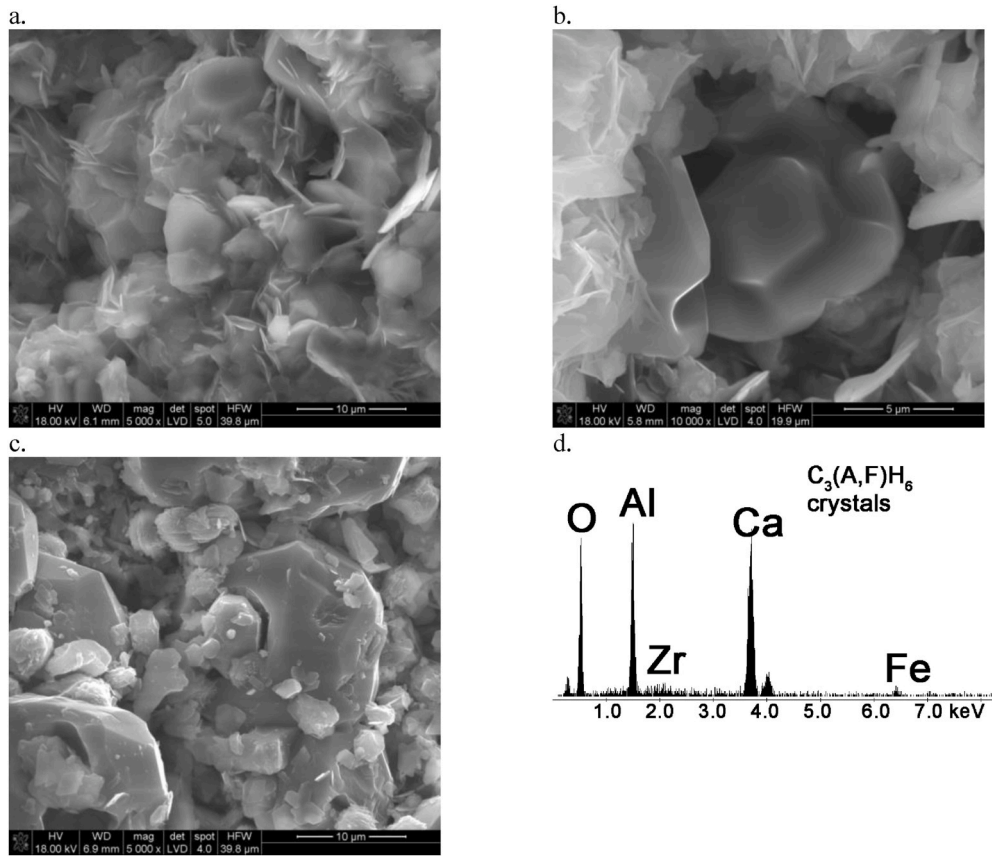


Fig. 9. SEM images of hydrated Fe-modified C-A-Z cement paste at 24.h (a–b) and 7.day (c). EDS spectrum of $C_3(A,F)H_6$ crystals (d).

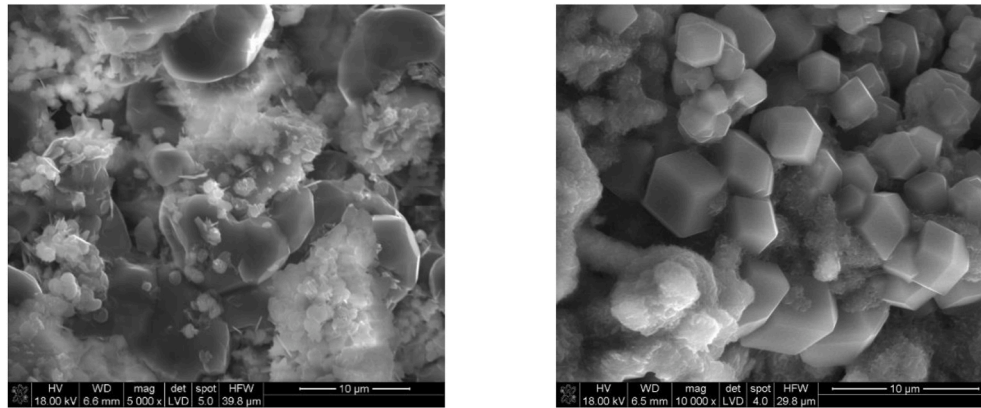


Fig. 10. SEM images of hydrated reference pure C-A-Z (a) and CAC (b) cement pastes at 3.day.

of the 100 % peak around 2θ of 39.223° (d-spacing 2.29500 \AA , ICDD Card No. 00-024-0217) at 24. h of hydration. The conversion reactions were evidenced by the decrease in peak height belonging to C_4AH_19 and C_2AH_8 , while the peak height of C_3AH_6 increased. At the same time, the conversion reactions produce $Al(OH)_3$ as the crystalline phase at 7. day of hydration. It was demonstrated based on the significant peak at close to $18.300^\circ 2\theta$ position (d-spacing 4.84406 \AA , ICSD Card No. 98-003-6233). As it can be seen in Fig. 7b, the C_3AH_6 XRD peak position and intensity are affected by both Fe substitution and curing period of cement pastes. Firstly, the intensity of the C_3AH_6 XRD peak for an undoped sample is higher than that of for Fe-containing paste at the same curing times. Results showed also that the intensity of the C_3AH_6 XRD peak increased with the curing time. This could be explained by the greater extent of crystallization of C_3AH_6 in curing processes proceeding

with time. Secondly, the diffraction peak from the Fe-substituted C_3AH_6 tends to shift toward the lower 2θ angle compared to the position of the strongest peak for the undoped C_3AH_6 . The XRD pattern also indicates a weak peak centered around 2θ of 11.681° (7.57000 \AA), which is the dominant peak for $C_3A \cdot CaCO_3 \cdot 11H_2O$ (ICDD Card No. 00-036-0377) formed at 24.h of hydration.

The DSC-TG-EGA(MS) curves of the hardened Fe-modified C-A-Z cement paste at 15. min, 30. min, 1 h, 24 h, 3 days, and 7 days are presented in Fig. 8a and b. It could be observed that each sample revealed some peaks with similar temperature positions at ages between 15 min and 1 h, and between 24 h and 7 days. The ionic current scans in the mass spectra at the temperature of $25\text{--}270^\circ \text{C}$ showed three signals at m/z 18 (Fig. 8b) related to the H_2O^+ species [78,79]. The EGA(MS) peak near $254\text{--}267^\circ \text{C}$ is ascribed to C_4AH_19 [80–82]. These results showed

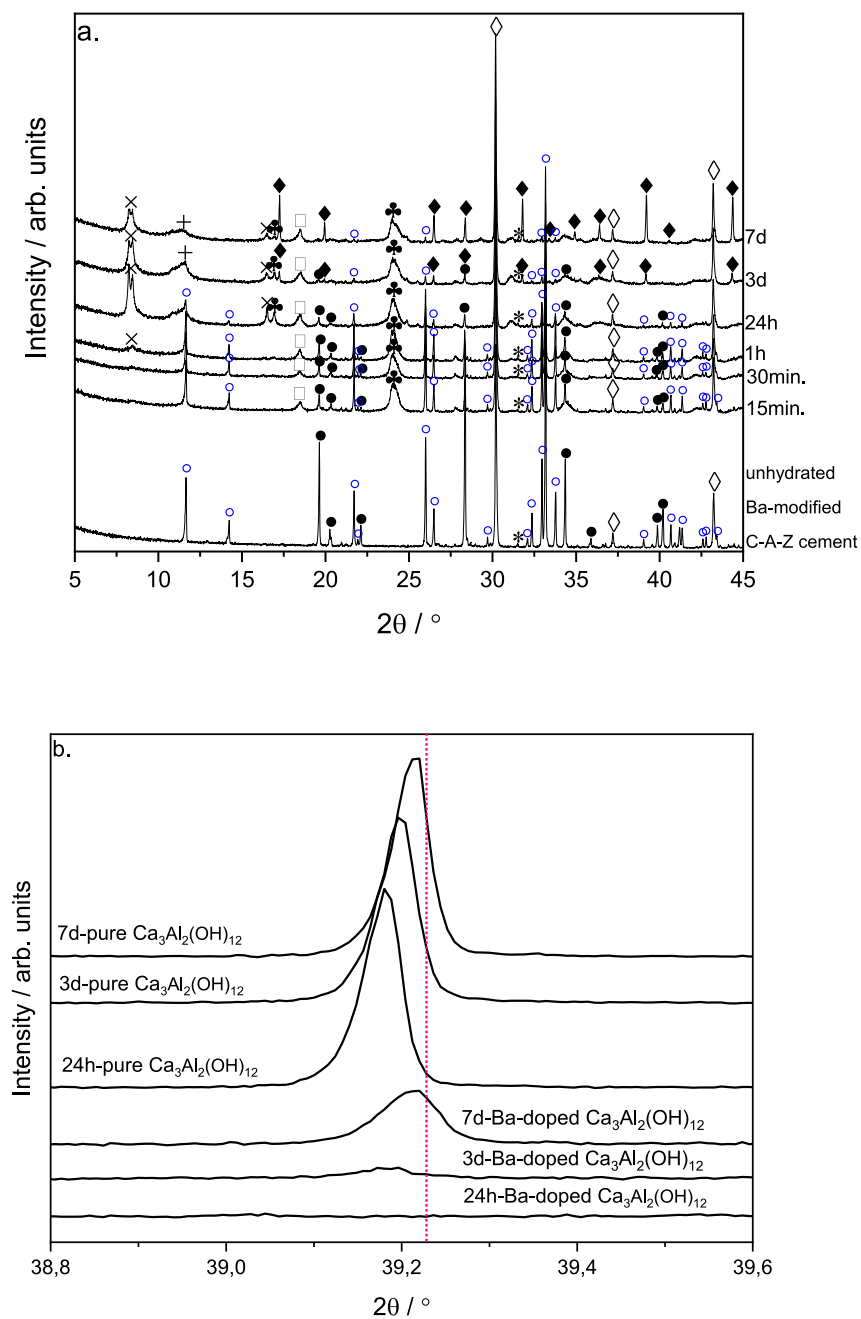


Fig. 11. X-ray diffraction patterns of Ba-modified C-A-Z cement when hydrated between 15 min and 7 days (a). Cement paste prepared with $w/c = 1.0$ cured at 50°C . The markers indicate the reference peak positions of reference data for all phases identified: $^\circ\text{Ca}_7\text{ZrAl}_6\text{O}_{18}$ (ICSD Card No. 98-015-7989), $^*\text{CaZrO}_3$ (ICSD Card No. 98-009-7466), $\blacklozenge\text{Ca}_3\text{Al}_2(\text{OH})_{12}$ (ICDD Card No. 00-024-0217), $\times\text{3CaO}\cdot\text{Al}_2\text{O}_3\cdot\text{Ca}(\text{OH})_2\cdot 18\text{H}_2\text{O}$ (ICDD Card No. 00-042-0487)/ $\text{Ca}_2\text{Al}_2\text{O}_5\cdot 8\text{H}_2\text{O}$ (ICDD Card No. 00-045-0564), $+ \text{C}_3\text{A}\cdot\text{CaCO}_3\cdot 11\text{H}_2\text{O}$ (ICDD Card No. 00-036-0377), $\nabla\text{Al}(\text{OH})_3$ (ICSD Card No. 98-003-6233), $\blacklozenge\text{Ba}_2\text{Al}_2\text{O}_5\cdot 2\text{H}_2\text{O}$ (ICDD Card No. 00-044-0473), $\diamond\text{Ba}_{0.8}\text{Ca}_{0.2}\text{ZrO}_3$ (ICSD Card No. 98-009-7473), $\bullet\text{BaAl}_2\text{O}_4$ (ICSD Card No. 98-001-5728). Position 2θ of the "100 % peak" of undoped $\text{Ca}_3\text{Al}_2(\text{OH})_{12}$ according to the ICDD Card No. 00-024-0217 marked as a pink vertical line (b). The undoped $\text{Ca}_3\text{Al}_2(\text{OH})_{12}$ was synthesized through the $\text{Ca}_7\text{ZrAl}_6\text{O}_{18}$ hydration.

clearly distinguishable thermal transitions below 200°C due to the possible decomposition of amorphous tetracalcium aluminum carbonate hydrate, $\text{C}_3\text{A}\cdot\text{CaCO}_3\cdot 11\text{H}_2\text{O}$ coinciding with the possible decomposition of amorphous dicalcium aluminate hydrate, C_2AH_8 , and the possible decomposition of AH_3 -gel. Two hydrates $\text{C}_4\text{ACH}_{11}$ and C_2AH_8 do indeed give decomposition peaks in the same temperature range of $160\text{--}200^\circ\text{C}$ [83]. Similar decomposition temperatures were proved from the DSC

curves. It was shown that the chemically bound water obtained using TG corresponds to the total mass losses of about 17.4, 19.0, and 21.2 % measured in the examined temperature range at 15 min., 30 min, and 1 h of curing, respectively (Fig. 7a). This indicates that the water was gradually consumed with the continuous hydration of cement and the cement particles were replaced with hydrates. Similarly, the DSC-TG-EGA(MS) was successfully used to identify the products formed

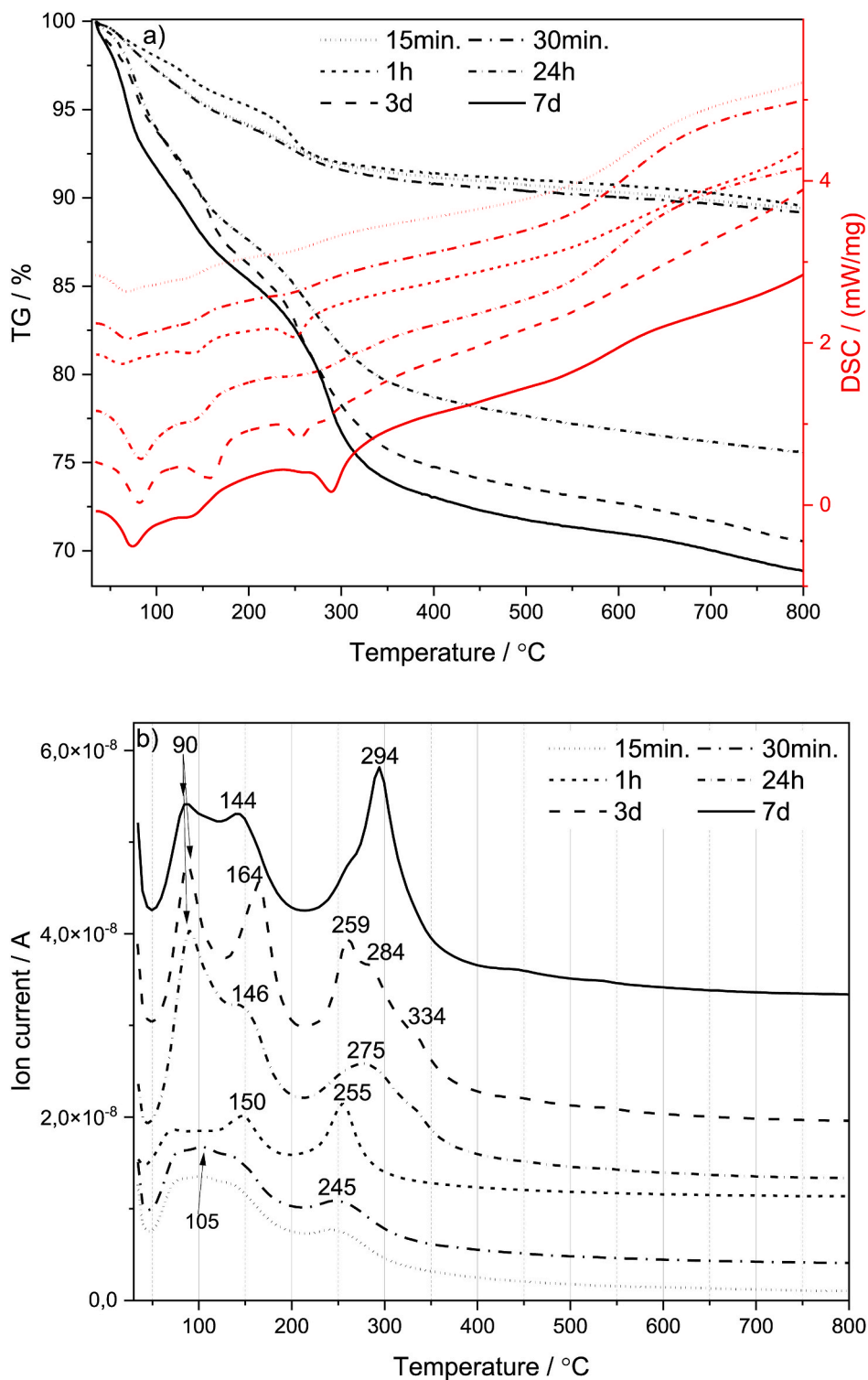


Fig. 12. The TG and DSC curves summarizing the thermal behavior of the Ba-modified C-A-Z cement paste when heated from 30 to 800 °C at 10 °C/min (a). Gas evolution curves for representative mass spectroscopic ion fragment of H_2O^+ ($m/z = 18$) vapors during the thermal decomposition of the Ba-modified C-A-Z cement paste (b). Cement paste prepared with $w/c = 1.0$ cured at 50 °C. Hydration at ages 15 min to 7 days.

in cement paste that was cured for different periods between 24 h and 7 days. The DSC and EGA(MS) curves appear endothermic or H_2O emission peak at ca. 296 °C due to the crystalline hydrate C_3AH_6 decomposition [84]. This corresponds to the dehydration process with a total mass loss between 24.1 and 28.0 % for the cement paste cured between 24 h and 7 days, respectively.

In order to characterize both the effect of Fe doping and the curing

time on the studied cement paste in more detail, their microstructure was observed with SEM-EDS. The SEM images of the Fe-modified C-A-Z cement paste specimens obtained after 24 h and 7 d of hydration are illustrated in Fig. 9a and b and Fig. 9c, respectively. The representative EDS spectrum of the $\text{C}_3(\text{A},\text{F})\text{H}_6$ crystals is shown in Fig. 9d. This study focused also on the microstructure of Fe-modified C-A-Z cement paste in comparison with the reference pure C-A-Z and CAC pastes, presented in

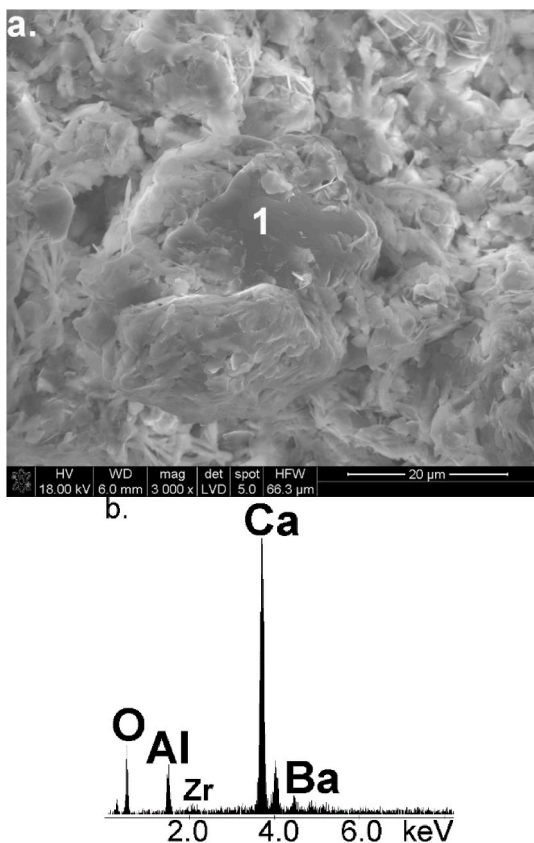


Fig. 13. SEM images of hydrated Ba-modified C-A-Z cement paste at 7.d (a). EDS spectrum of Ba-doped C_3AH_6 crystals (b).

Fig. 10a and b, respectively. As a general rule it can be stated that SEM analysis of changes in the morphology and microstructure of cement pastes allowed us to track the hydration progress observed mainly by changes in the C-A-H and C-(A,F)-H phases.

As presented in Fig. 9a and b, the hexagonal-shaped flake-like forms of C-(A,F)-H can be dominant phases formed in the Fe-modified C-A-Z cement paste. Nevertheless, some nuclei of $C_3(A,F)H_6$ hydrate can be seen in the center of the SEM image (Fig. 9b) after 24 h curing. Crystals of $C_3(A,F)H_6$ characterized by well-developed crystal faces (external surfaces) were formed after 7 days of curing (Fig. 9c). The EDS spectrum indicates that the synthesized Fe-doped C_3AH_6 mainly contains Ca, Al, Fe, Zr and O elements with a composition of Ca - 16.56 at %, Al - 14.20 at %, Fe - 0.96 at %, Zr - 0.36 at % and O - 67.92 at % (Fig. 9d).

Also, the SEM investigations revealed that C_3AH_6 prepared from different precursors have yielded different morphologies (Fig. 9c and 10a-b). Firstly, compared with cubic hydrate prepared from commercial CAC (Fig. 10b), a noticeable change can be observed that the C_3AH_6 made from C-A-Z cement caused the formation of larger irregular polyhedra C_3AH_6 hydrate, ca. 10–15 μm (Fig. 10a). The presence of well crystalline cubic and granular crystals of C_3AH_6 ca. 3–5 μm, similar to that of presented in Fig. 10b has also been reported by P. Barnes and J. Bensted and given in Ref. [85]. Secondly, the most noticeable change in the mean crystal size of cubic hydrate occurred, when comparing both undoped CAC and C-A-Z cement samples (Fig. 10a and b), with the Fe-modified C-A-Z one (Fig. 9c), which suggests that the incorporation of iron into a hydrate structure caused the formation of large irregular crystalline polyhedral hydrates of $C_3(A,F)H_6$, ca. 20 μm.

3.2.2. Ba-modified C-A-Z cement

The XRD patterns of un-hydrated Ba-modified C-A-Z cement and its paste hydrated between 15 min and 7 days are shown in Fig. 11. For the un-hydrated sample, the cement clinker minerals were identified as

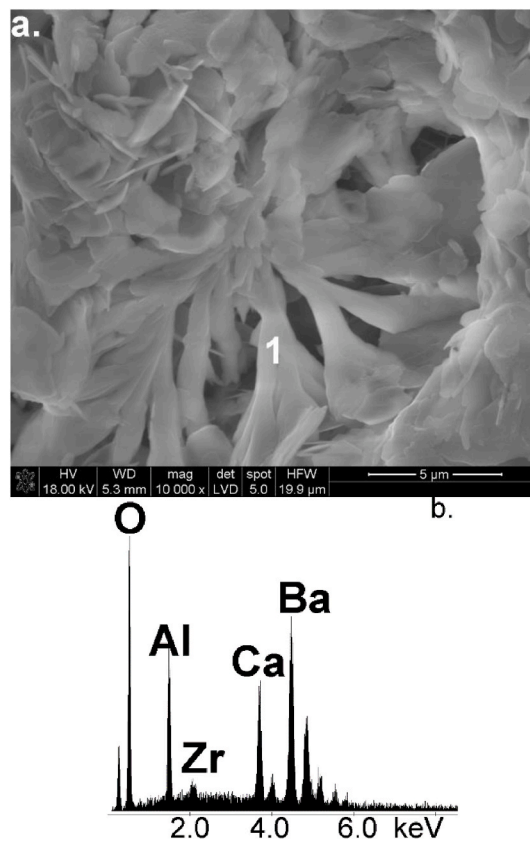


Fig. 14. SEM images of hydrated Ba-modified C-A-Z cement paste at 7.d (a). EDS spectrum of elongated crystals of calcium-barium-aluminate hydrates (b).

reported before (Fig. 4). The XRD patterns of the cement hydrated at 50 °C show a complex nature of the formation of the hydration products. At the very early stage of hydration, the main hydration products obtained from hydration of neat Ba-modified C-A-Z cement-based paste are two hydrates $Ba_2Al_2O_5 \cdot 2H_2O$ and $Al(OH)_3$ formed between 15 and 30 min, as shown in Fig. 11a. The 100 % main diffraction peaks corresponding to the $Ba_2Al_2O_5 \cdot 2H_2O$ and $Al(OH)_3$ appear at 2θ of 23.517–24.265° (d-spacing 3.78000–3.66500 Å) and 18.300° (d-spacing 4.84406 Å) which are in very good agreement with ICDD Card No. 00-044-0473 and ICSD Card No. 98-003-6233 for barium aluminate hydrate and aluminum hydroxide, respectively. Starting from the 1st h of hydration, peaks of C_4AH_{19} or C_2AH_8 were recognized. As mentioned before, the diffraction peaks belonging to C_4AH_{19} coincide with those of C_2AH_8 , suggesting that both hydrates were formed. Hence, a clear distinction between these two hydration products is difficult at this stage. The 100 % main diffraction peaks corresponding to the C_4AH_{19} or C_2AH_8 hydrates appear at 2θ of 10.64350° (d-spacing 8.301 Å) and 10.81270° (d-spacing 8.170 Å) which are in very good agreement with ICDD Card No. 00-042-0487 and ICSD Card No. 00-045-0564 for C_4AH_{19} and C_2AH_8 , respectively. This confirms that at the very early stage of hydration, Ba-doped $Ca_7ZrAl_6O_{18}$ reacts very violently with water, resulting in an immediate formation of the Ca-Al hydrates. Nevertheless, these results showed also that the hydration of Ba-doped $Ca_7ZrAl_6O_{18}$ in the Ba-doped C-A-Z blended paste was significantly delayed in comparison with the Fe-doped $Ca_7ZrAl_6O_{18}$ in the Fe-doped C-A-Z blended paste.

It's worth noting also that during the first few minutes or hours of hydration, the high temperature increases the precipitation rate of hydration products but it does not produce direct formation of C_3AH_6 . Also, it can be observed that the intensity of $Ca_7ZrAl_6O_{18}$ and $BaAl_2O_4$ -peaks decreases due to reactions with water. In the Ba-modified cement paste, the barium incorporation determines the appearance of peaks

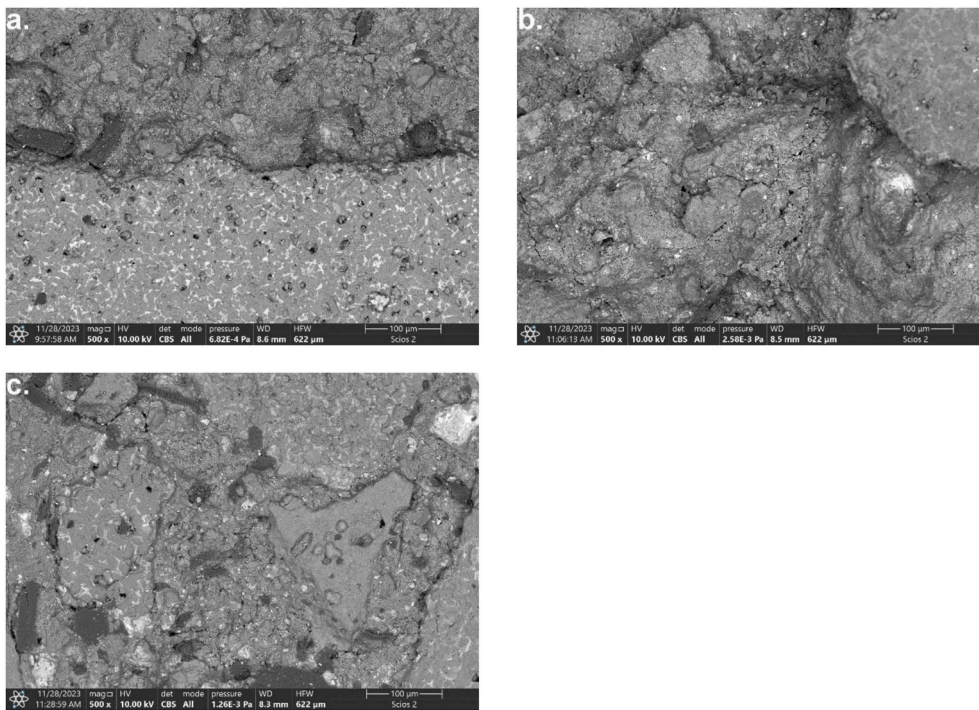


Fig. 15. a-c Overview of SEM images at $\times 500$ magnification of the CAC-(C-A), Ba-doped C-A-Z (C-B) and Fe-doped C-A-Z (C-C) cements-containing bauxite-based concretes after heat treatment at $110\text{ }^{\circ}\text{C}$, respectively.

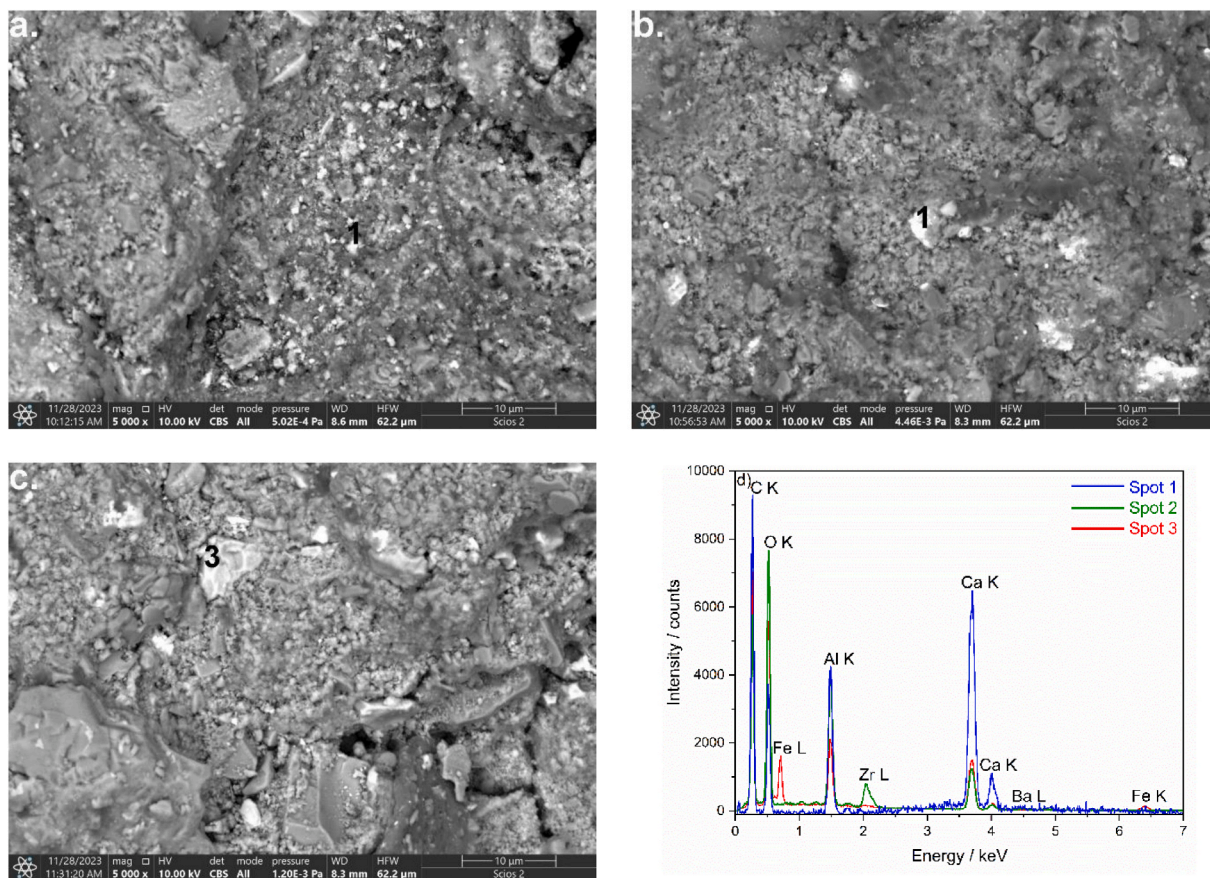


Fig. 16. a-c Detailed SEM images at $\times 5000$ magnification of the CAC-(C-A), Ba-doped C-A-Z (C-B) and Fe-doped C-A-Z (C-C) cements-containing bauxite-based concretes after heat treatment at $110\text{ }^{\circ}\text{C}$, respectively. EDS analyses from the white inclusions visible in fine-grained matrix designed as points 1-3 in Fig. 15a-c (d).

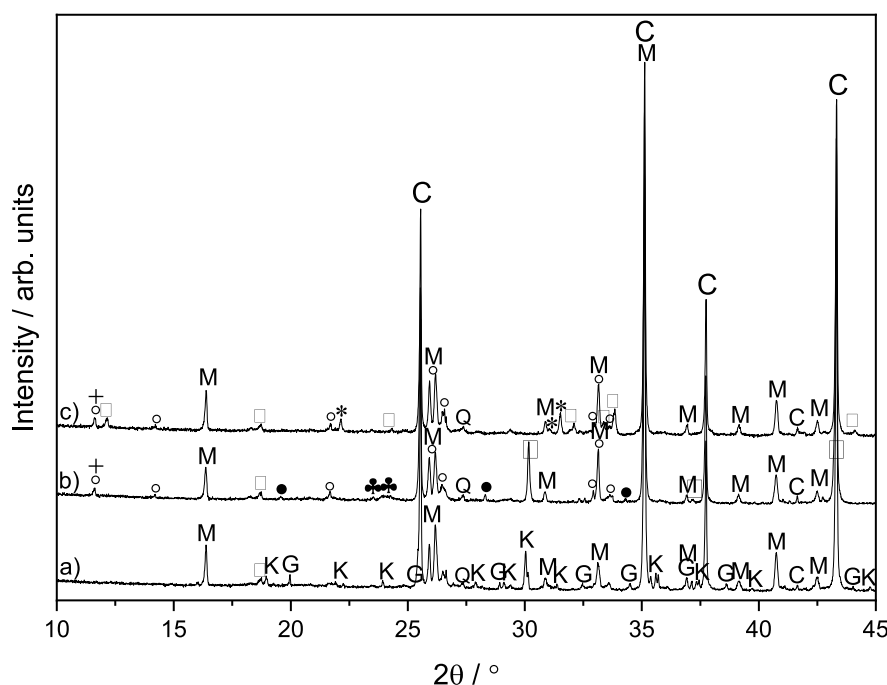


Fig. 17. The XRD pattern of the a) CAC-(C-A), b) Ba-doped C-A-Z (C-B), and c) Fe-doped C-A-Z (C-C) cements-containing bauxite-based concretes after heat treatment at 110 °C. The symbols indicate the different phases: C-corundum (Al₂O₃; ICDD Card No. 01-071-1123), M-mullite (Al_{1.83}Si_{1.08}O_{4.85}, ICSD Card No.98-004-3298), Q-quartz (SiO₂, ICSD Card No. 98-001-6333), K-CaAl₂O₄ (ICSD Card No. 98-018-0997), G-CaAl₄O₇ (ICSD Card No. 98-004-4519), ∇Al(OH)₃ (ICSD Card No. 98-003-6233), °Ca₇ZrAl₆O₁₈ (ICSD Card No. 98-015-7989), ◊Ba_{0.8}Ca_{0.2}ZrO₃ (ICSD Card No. 98-009-7473), *BaAl₂O₄ (ICSD Card No. 98-001-5728), +C₃A·CaCO₃·11H₂O (ICDD Card No. 00-036-0377), ◆Ba₂Al₂O₅·2H₂O (ICDD Card No. 00-044-0473), ◐CaZrO₃ (ICSD Card No. 98-009-7466), ◑Ca₂AlFeO₅ (ICSD Card No. 98-009-7926).

Table 4

Elemental analysis of concrete materials at 25 °C after casting.

Sample	Element										Total
	O	Al	Ca	Fe	Ti	Na	Zr	Ba	H	Si	
	mas. %										
CAC-(C-A)	49.54	43.96	2.15	0.78	1.67	0.12	–	–	0.87	0.91	100
Ba-doped C-A-Z (C-B)	48.54	42.01	2.68	0.78	1.67	0.12	0.97	1.45	0.87	0.91	100
Fe-doped C-A-Z (C-C)	48.67	41.49	3.24	2.02	1.67	0.12	1.01	–	0.87	0.91	100

assigned to C₃AH₆ showing the delay in the formation of this hydrate due to the conversion of both C₄AH₁₉ and C₂AH₈. The conversion phenomena were evidenced by a decrease in the peak height corresponding to C₄AH₁₉ and C₂AH₈ while the peak height of C₃AH₆ increased. According to the results presented elsewhere [72], C₃AH₆ starts to precipitate at 24. h of hydration within the un-doped C₇A₃Z-based paste. According to these results, some part of Ba²⁺ reacted probably with Al(OH)₄ and the expected formation of Ba₂Al₂O₅·2H₂O could be clearly detected at 2θ value of 23.517–24.265° (d-spacing 3.78000–3.66500 Å) during the entire hydration process. It is observed that the main low-intensity peak of C₃AH₆ appears at 2θ value of 39.223° (d-spacing 2.29500 Å, ICDD Card No. 00-024-0217) at 3. day of hydration. As also can be seen in Fig. 11b, the C₃AH₆ XRD peak intensity is affected by the curing period and barium presence. The intensity of an XRD peak slowly increased with an increase in aging time between 3.d and 7.d. The XRD pattern also indicates a weak peak centered around 2θ of 11.681° (7.57000 Å), which is the dominant peak for C₃A·CaCO₃·11H₂O (ICDD Card No. 00-036-0377) formed at 3.d of hydration. This is in good agreement with the data published by other authors [86] revealing that the C₃AH₆ hydrate decomposes and calcium monocarboaluminate hydrate is formed.

The DSC-TG-EGA(MS) curves of the hardened Ba-modified C-A-Z

cement paste at 15. min, 30. min, 1 h, 24 h, 3 days and 7 days are shown in Fig. 12a and b. The results showed the typical weight loss areas related to the dehydration mainly of two hydrates Ba₂Al₂O₅·2H₂O and Al(OH)₃ formed between 15 and 30 min in the temperature ranges 50–150 °C and 200–300 °C with two maxima at ca. 105 °C and 245 °C in the MS curves of H₂O⁺ (18 m/z = 18), respectively, related to the decomposition of both barium aluminate hydrate and aluminum hydroxide. The mass spectra profile of H₂O⁺ at m/z = 18 derived from the Ba-doped C-A-Z cement paste after the first hour of curing exhibits broad peaks below 150 °C and an intense peak located at ca. 255 °C due to the C₄AH₁₉ hydrate decomposition [80–82]. Results gained using MS revealed, intensified release of water molecules from the heated Ba-doped C-A-Z cement paste cured for 24 h, 3 days, and 7 days at the temperature region below 200 °C and intense peaks in the range 250–350 °C. The peaks below 200 °C correspond to the possible decomposition of C₂AH₈, C₃A·CaCO₃·11H₂O, Ba₂Al₂O₅·2H₂O and AH₃-gel [87,88]. It was also noted that C₄AH₁₁ and C₂AH₈ do indeed give decomposition peaks in the same temperature range of 190–200 °C [83]. The intense and broad peak, due to the loss of water from C₃AH₆ and Al(OH)₃, appears from 3 days of hydration in the temperature range 260–350 °C. For the cement paste cured for 7 days, the mass spectra profile of H₂O⁺ at m/z = 18 is dominated by the maximum at 294 °C due

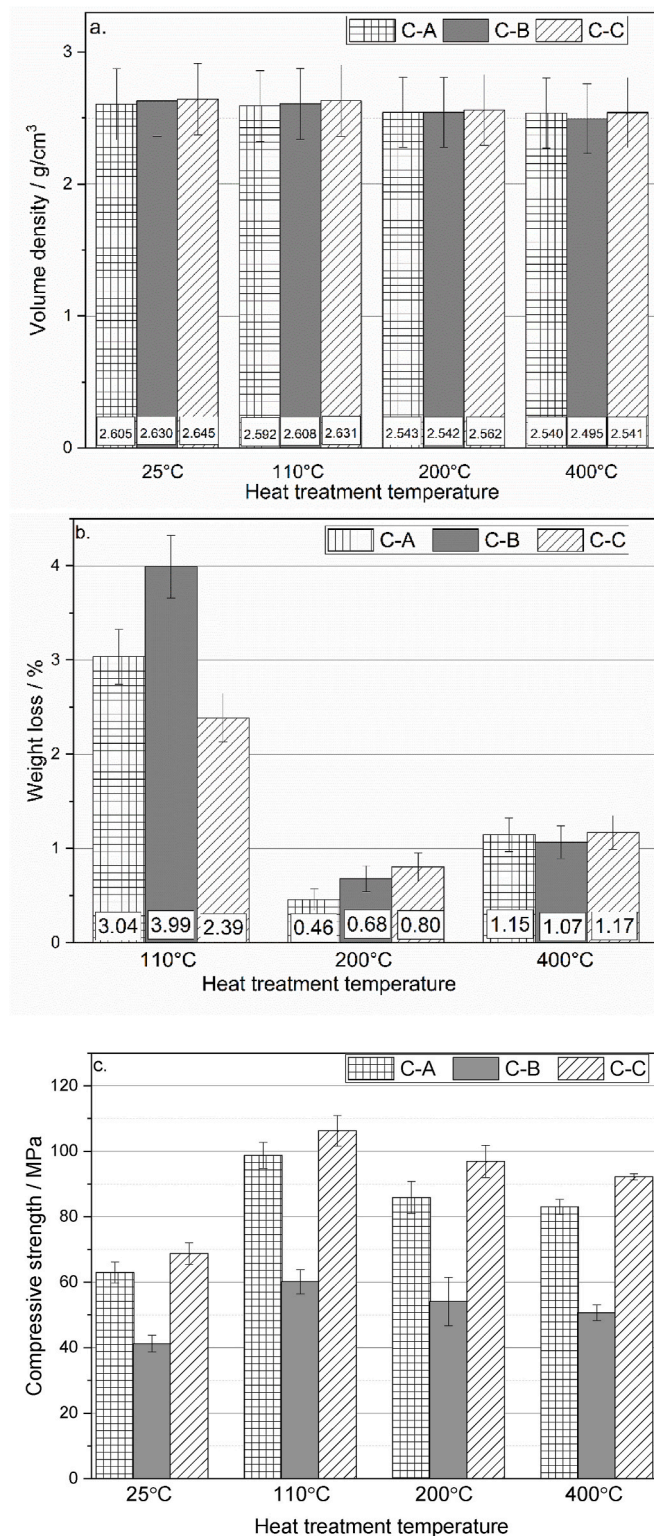


Fig. 18. Variation of the volumetric density of the CAC (C-A), Ba-doped C-A-Z (C-B), and Fe-doped C-A-Z (C-C) cements-containing bauxite-based concretes at elevated temperature (a), weight loss concretes at a temperature between 25 °C and 400 °C (b) and CCS of concretes at a temperature between 25 °C and 400 °C (c).

to C_3AH_6 decomposition [87]. Fig. 12a shows the thermogravimetric analysis of the hydrated and cured cement paste after 15. min., 30 min, 1 h, and 24 h, 3d, 7 days with a weight loss of ca. 10.5, and 24.4, 29.5, 31.1 %, respectively. The results from TG showed the typical weight loss

areas related to the elimination of the chemically bound water, which was a result of cement hydration.

The results of SEM analysis of morphological characteristics of the Ba-modified C-A-Z cement paste prepared at a water-to-solid weight ratio of 1.0 at the age of 7 days are presented in Figs. 13 and 14. The morphology of hydration products formed at 7. day of curing is influenced by the barium presence. The large crystals of C_3AH_6 doped with Ba (Fig. 13a and b) and elongated crystals of calcium-barium-aluminate hydrates (Fig. 14a and b) can be produced. Fig. 13b shows the EDS spectrum of the large trapezohedral-type C_3AH_6 crystals \approx 3-5 times the size of the C_3AH_6 crystals produced within CAC-based paste (Fig. 10b). These crystals contain elements including mainly Ca, Al, and O. This EDS microanalysis also shows very low barium concentration. According to the EDS microanalysis, the elongated crystals (Fig. 14a and b) are calcium-barium-aluminate hydrates. The EDS spectrum confirms the presence of high concentrations of Ca, Ba, Al, and O in the sample.

3.3. Concrete materials

3.3.1. SEM-EDS and XRD characterizations of concretes

The results of the microstructural observations of the concrete samples using the SEM-EDS technique are shown in Fig. 15a–c and 16a–d. The analysis was performed on the polished cross sections of the CAC (C-A), Ba-doped C-A-Z (C-B) and Fe-doped C-A-Z (C-C) cements-containing bauxite-based concretes after heat treatment at 110 °C. It is well understood that the type of cement affects the physical and mechanical properties of concretes. In the case of all samples, it was found from the image that there were coarse aggregate calcined bauxite and fine-grained matrix. Furthermore, the interfacial transition zone between the aggregates and bulk cement-containing matrix seems to be slightly porous and contains cracks. It can be also stated that the concrete matrix is composed of residual unhydrated and dehydrated cements, other reactive fillers, and unreactive fillers. It can be seen from the detailed SEM microstructure of each concrete material presented in Fig. 16a–c, that numerous light grey areas are uniformly distributed in the fine-grained matrix. At higher magnification and after the EDS analysis, as shown in Fig. 16a–d, it is clear that the white inclusions within the fine-grained matrix mainly consists of Ca, Al and O (C-A sample, Fig. 16a-Spot 1 and Fig. 16d), Ca, Ba, Zr, Al and O (C-B sample, Fig. 16b-Spot 2 and Fig. 16d) and Ca, Fe, Al and O (C-C sample, Fig. 16c-Spot 3 and Fig. 16d). As regards the white small (Fig. 16a-Spot 1) or larger particles (Fig. 16a-b-Spots 2-3), for which EDS microprobe evidenced the composition presented previously, these seem to be made up of unhydrated cement residues or partly dehydrated cement grains.

Regarding concrete samples C-A, C-B, and C-C after heat treatment at 110 °C, X-ray diffraction was employed to characterize the phase composition of concrete specimens containing CAC, Ba- and Fe-modified C-A-Z cements. The results are shown in Fig. 17a–c. As this type of concrete material was made of bauxite aggregates, bauxite fume, and reactive alumina, the XRD diffraction patterns show evidence of the presence of the majority of crystalline phases of corundum (Al_2O_3 ; ICDD Card No. 01-071-1123), mullite ($Al_{1.83}Si_{1.08}O_{4.85}$, ICSD Card No.98-004-3298) and quartz (SiO_2 , ICSD Card No. 98-001-6333) in all samples investigated. Since the C-A sample was bonded with calcium aluminate cement, the XRD diffraction pattern of sample C-A shows evidence of the presence of secondary crystalline phases of calcium monoaluminate ($CaAl_2O_4$; ICSD Card No. 98-018-0997) and calcium dialuminate ($CaAl_4O_7$; ICSD Card No. 98-004-4519) as unhydrated residues (Fig. 17a). The crystalline component of the cementing matrix identified by XRD was $Al(OH)_3$ (ICSD Card No. 98-003-6233), only. As two other concrete materials were bonded with the Ba-doped C-A-Z (C-B) or Fe-doped C-A-Z (C-C) cements many different secondary phases were found. Besides corundum, mullite, and quartz, the C-B sample contains also residues of unhydrated phases $BaAl_2O_4$ (ICSD Card No. 98-001-5728) and $Ca_7ZrAl_6O_{18}$ (ICSD Card No. 98-015-7989), and other phase from the starting cement such as $Ba_{0.8}Ca_{0.2}ZrO_3$ (ICSD Card No.

Table 5ASummary of the obtained values of parameters describing the γ radiation shielding properties of material A before drying and annealing.

SAMPLE A								
Energy/keV	μ /cm ⁻¹	$\Delta\mu$ /cm ⁻¹	l_{HVL} /cm	l_{HVL} /cm	μ_m /cm ⁻¹	μ_m /cm ⁻¹	σ_a /b/atom	$\Delta\sigma_a$ /b/atom
81	0.187	0.016	3.71	0.31	0.072	0.006	2.09	0.18
122	0.499	0.065	1.39	0.18	0.192	0.025	5.55	0.72
245	0.189	0.039	3.66	0.76	0.073	0.015	2.11	0.44
344	0.269	0.007	2.58	0.07	0.103	0.003	2.99	0.08
356	0.208	0.021	3.34	0.34	0.080	0.008	2.31	0.23
511	0.197	0.017	3.52	0.31	0.076	0.007	2.19	0.19
662	0.209	0.005	3.32	0.09	0.080	0.002	2.32	0.06
779	0.184	0.008	3.77	0.16	0.070	0.003	2.04	0.09
964	0.215	0.002	3.23	0.02	0.082	0.001	2.39	0.02
1173	0.149	0.000	4.65	0.01	0.057	0.000	1.66	0.01
1274	0.132	0.011	5.23	0.42	0.051	0.004	1.47	0.12
1333	0.143	0.002	4.84	0.05	0.055	0.001	1.59	0.02
1408	0.155	0.014	4.47	0.39	0.059	0.005	1.72	0.15

Table 5BSummary of the obtained values of parameters describing the γ radiation shielding properties of material B before drying and annealing.

SAMPLE B								
Energy/keV	μ /cm ⁻¹	$\Delta\mu$ /cm ⁻¹	l_{HVL} /cm	l_{HVL} /cm	μ_m /cm ⁻¹	μ_m /cm ⁻¹	σ_a /b/atom	$\Delta\sigma_a$ /b/atom
81	0.172	0.032	4.02	0.76	0.066	0.012	1.94	0.36
122	0.453	0.043	1.53	0.15	0.172	0.016	5.08	0.48
245	0.168	0.008	4.13	0.18	0.064	0.003	1.88	0.08
344	0.328	0.025	2.11	0.16	0.125	0.009	3.68	0.28
356	0.192	0.004	3.61	0.08	0.073	0.002	2.15	0.05
511	0.219	0.005	3.16	0.07	0.083	0.002	2.46	0.05
662	0.205	0.005	3.39	0.08	0.078	0.002	2.30	0.06
779	0.151	0.007	4.58	0.23	0.058	0.003	1.70	0.08
964	0.115	0.002	6.01	0.11	0.044	0.001	1.29	0.02
1173	0.148	0.002	4.69	0.05	0.056	0.001	1.66	0.02
1274	0.146	0.005	4.76	0.18	0.055	0.002	1.63	0.06
1333	0.139	0.002	5.00	0.07	0.053	0.001	1.56	0.02
1408	0.202	0.016	3.44	0.28	0.077	0.006	2.26	0.18

Table 5CSummary of the obtained values of parameters describing the γ radiation shielding properties of material C before drying and annealing.

SAMPLE C								
Energy/keV	μ /cm ⁻¹	$\Delta\mu$ /cm ⁻¹	l_{HVL} /cm	l_{HVL} /cm	μ_m /cm ⁻¹	μ_m /cm ⁻¹	σ_a /mb/atom	$\Delta\sigma_a$ /mb/atom
81	0.176	0.012	3.94	0.27	0.067	0.005	19.7	1.3
122	0.460	0.006	1.51	0.02	0.175	0.002	51.5	0.6
245	0.173	0.027	4.00	0.61	0.066	0.010	19.4	3.0
344	0.330	0.044	2.10	0.28	0.126	0.017	37.0	4.9
356	0.176	0.023	3.94	0.51	0.067	0.009	19.7	2.6
511	0.226	0.005	3.07	0.07	0.086	0.002	25.3	0.6
662	0.208	0.008	3.33	0.12	0.079	0.003	23.3	0.9
779	0.181	0.003	3.82	0.07	0.069	0.001	20.3	0.4
964	0.124	0.018	5.60	0.83	0.047	0.007	13.9	2.1
1173	0.157	0.004	4.42	0.13	0.060	0.002	17.5	0.5
1274	0.154	0.004	4.51	0.12	0.058	0.002	17.2	0.5
1333	0.149	0.005	4.65	0.16	0.057	0.002	16.7	0.6
1408	0.178	0.004	3.91	0.08	0.067	0.001	19.9	0.4

98-009-7473) (Fig. 17b). The crystalline components of the cementing matrix identified by XRD were Al(OH)₃ (ICSD Card No. 98-003-6233), C₃A·CaCO₃·11H₂O (ICDD Card No. 00-036-0377) and Ba₂Al₂O₅·2H₂O (ICDD Card No. 00-044-0473). The XRD measurements show that C-C sample contains a mixture of corundum, mullite and quartz from fillers, and Ca₇ZrAl₆O₁₈ (ICSD Card No. 98-015-7989), Ca₂AlFeO₅ (ICSD Card No. 98-009-7926) and CaZrO₃ (ICSD Card No. 98-009-7466) from cement (Fig. 17c). Additionally, the crystalline components of the cementing matrix identified by XRD were Al(OH)₃ (ICSD Card No. 98-003-6233) and C₃A·CaCO₃·11H₂O (ICDD Card No. 00-036-0377).

3.3.2. Chemical, physical and mechanical properties of concrete

The chemical composition of concretes after casting and curing at 25 °C is presented in Table 4. Fig. 18 a and b present the variation of the volumetric density of the CAC-(C-A), Ba-doped C-A-Z (C-B), and Fe-doped C-A-Z (C-C) cements-containing bauxite-based concretes at elevated temperature and the weight loss concretes at a temperature between 25 °C and 400 °C, respectively. The cold crushing strength results against varied heat-treatment temperatures of concretes are presented in Fig. 18c.

As can be seen from Fig. 18, all concretes have a density reaching the

Table 6A
 γ radiation shielding parameters of material A after drying at 110 °C.

SAMPLE A								
Energy/keV	μ /cm ⁻¹	$\Delta\mu$ /cm ⁻¹	I_{HVL} /cm	I_{HVL} /cm	μ_m /cm ⁻¹	μ_m /cm ⁻¹	σ_a /b/atom	$\Delta\sigma_a$ /b/atom
122	0.379	0.013	1.83	0.06	0.146	0.005	4.50	0.15
245	0.593	0.202	1.17	0.40	0.229	0.078	7.04	2.40
344	0.271	0.006	2.56	0.06	0.104	0.002	3.22	0.07
511	0.200	0.004	3.47	0.07	0.077	0.002	2.38	0.05
662	0.199	0.006	3.49	0.10	0.077	0.002	2.36	0.07
779	0.180	0.010	3.84	0.21	0.070	0.004	2.14	0.12
964	0.165	0.012	4.20	0.29	0.064	0.004	1.96	0.14
1086	0.174	0.010	3.98	0.22	0.067	0.004	2.07	0.11
1112	0.166	0.007	4.17	0.18	0.064	0.003	1.98	0.09
1173	0.150	0.002	4.61	0.07	0.058	0.001	1.79	0.03
1274	0.145	0.006	4.77	0.20	0.056	0.002	1.73	0.07
1333	0.146	0.001	4.76	0.04	0.056	0.001	1.73	0.02
1408	0.134	0.009	5.17	0.36	0.052	0.004	1.59	0.11

Table 6B
 γ radiation shielding parameters of material B after drying at 110 °C.

SAMPLE B								
Energy/keV	μ /cm ⁻¹	$\Delta\mu$ /cm ⁻¹	I_{HVL} /cm	I_{HVL} /cm	μ_m /cm ⁻¹	μ_m /cm ⁻¹	σ_a /b/atom	$\Delta\sigma_a$ /b/atom
122	0.417	0.009	1.66	0.03	0.160	0.003	5.14	0.11
245	0.515	0.072	1.35	0.19	0.198	0.028	6.34	0.88
344	0.268	0.005	2.59	0.05	0.103	0.002	3.29	0.07
511	0.202	0.002	3.43	0.04	0.077	0.001	2.49	0.03
662	0.189	0.001	3.68	0.02	0.072	0.000	2.32	0.02
779	0.174	0.012	3.98	0.27	0.067	0.005	2.14	0.15
964	0.163	0.008	4.24	0.20	0.063	0.003	2.01	0.10
1086	0.152	0.015	4.57	0.46	0.058	0.006	1.86	0.19
1112	0.169	0.012	4.10	0.29	0.065	0.005	2.08	0.15
1173	0.143	0.002	4.83	0.08	0.055	0.001	1.77	0.03
1274	0.138	0.001	5.02	0.05	0.053	0.001	1.70	0.02
1333	0.137	0.001	5.05	0.05	0.053	0.001	1.69	0.02
1408	0.133	0.007	5.23	0.29	0.051	0.003	1.63	0.09

Table 6C
 γ radiation shielding parameters of material C after drying at 110 °C.

SAMPLE C								
Energy/keV	μ /cm ⁻¹	$\Delta\mu$ /cm ⁻¹	I_{HVL} /cm	I_{HVL} /cm	μ_m /cm ⁻¹	μ_m /cm ⁻¹	σ_a /b/atom	$\Delta\sigma_a$ /b/atom
122	0.379	0.012	1.83	0.06	0.144	0.005	4.45	0.14
245	0.639	0.101	1.08	0.17	0.243	0.038	7.50	1.18
344	0.265	0.005	2.62	0.05	0.101	0.002	3.11	0.06
511	0.209	0.002	3.31	0.03	0.080	0.001	2.46	0.02
662	0.191	0.002	3.62	0.04	0.073	0.001	2.25	0.03
779	0.192	0.002	3.61	0.04	0.073	0.001	2.25	0.03
964	0.170	0.004	4.07	0.10	0.065	0.002	2.00	0.05
1086	0.154	0.006	4.51	0.17	0.058	0.002	1.80	0.07
1112	0.159	0.011	4.35	0.29	0.061	0.004	1.87	0.12
1173	0.149	0.001	4.65	0.04	0.057	0.000	1.75	0.01
1274	0.144	0.001	4.81	0.04	0.055	0.000	1.69	0.01
1333	0.140	0.001	4.94	0.03	0.053	0.000	1.65	0.01
1408	0.136	0.004	5.08	0.13	0.052	0.001	1.60	0.04

value of nearly 2.6 g/cm³ at the ambient temperature of 25 °C. According to Standard BS EN 206-1 2001, the density of shielding concretes should be higher than 2.6 g/cm³ [89]. With the increase in temperature to 200 and 400 °C, the density of the concretes decreased. The highest density was measured after the samples were exposed to 600 °C for concretes containing the Fe-doped C-A-Z cement.

The weight loss of the concrete specimens for temperature increases at temperatures of 25, 200, and 400 °C for each mix is depicted in Fig. 18. As can be seen, the significant weight loss for the concrete samples was obtained at 400 °C which is in very good agreement with

the DSC-TG-EGA(MS) results, where the maximum water release peak occurs between 250 and 300 °C and is connected with the release of chemically bound water (crystal water) in hydrates (Figs. 8 and 12). At the temperature of 110 °C, the maximum weight loss is associated mainly with the evaporation of the capillary water and the physically adsorbed water (gel water).

In terms of mechanical properties at 110 °C, the C-A, C-B, and C-C concretes exhibit increased mechanical strength by ca. 57, 46 and 55 % of the initial values measured at 25 °C, respectively (Fig. 18c). The C-A, C-B, and C-C starting concretes had the CCS of 63, 41 and 69 MPa at

Table 7A
 γ radiation shielding parameters of concrete A after annealing at 400 °C.

SAMPLE A								
Energy/keV	μ /cm ⁻¹	$\Delta\mu$ /cm ⁻¹	I_{HVL} /cm	I_{HVL} /cm	μ_m /cm ⁻¹	μ_m /cm ⁻¹	σ_a /b/atom	$\Delta\sigma_a$ /b/atom
122	0.39	0.01	1.777	0.046	0.154	0.004	4.90	0.13
245	0.334	0.016	2.1	0.1	0.131	0.006	4.20	0.20
344	0.271	0.011	2.56	0.11	0.107	0.004	3.41	0.14
511	0.236	0.013	2.94	0.16	0.093	0.005	2.97	0.16
662	0.216	0.024	3.21	0.36	0.085	0.009	2.71	0.30
779	0.201	0.012	3.45	0.21	0.079	0.005	2.53	0.15
964	0.166	0.008	4.18	0.21	0.065	0.003	2.09	0.10
1086	0.167	0.023	4.15	0.57	0.066	0.009	2.1	0.3
1112	0.17	0.012	4.1	0.3	0.067	0.005	2.14	0.15
1173	0.15	0.006	4.6	0.2	0.059	0.002	1.88	0.08
1274	0.159	0.019	4.36	0.52	0.063	0.007	2.00	0.24
1333	0.143	0.008	4.85	0.27	0.056	0.003	1.80	0.10
1408	0.137	0.009	5.06	0.33	0.054	0.004	1.72	0.11

Table 7B
 γ radiation shielding parameters of concrete B after annealing at 400 °C.

SAMPLE B								
Energy/keV	μ /cm ⁻¹	$\Delta\mu$ /cm ⁻¹	I_{HVL} /cm	I_{HVL} /cm	μ_m /cm ⁻¹	μ_m /cm ⁻¹	σ_a /b/atom	$\Delta\sigma_a$ /b/atom
122	0.425	0.023	1.63	0.09	0.170	0.009	5.70	0.31
245	0.38	0.01	1.82	0.05	0.152	0.004	5.09	0.13
344	0.279	0.007	2.48	0.06	0.112	0.003	3.74	0.09
511	0.213	0.012	3.25	0.18	0.085	0.005	2.85	0.16
662	0.2	0.01	3.47	0.17	0.080	0.004	2.68	0.13
779	0.187	0.007	3.71	0.14	0.075	0.003	2.51	0.09
964	0.17	0.01	4.08	0.24	0.068	0.004	2.28	0.13
1086	0.154	0.023	4.50	0.67	0.062	0.009	2.06	0.31
1112	0.167	0.007	4.15	0.18	0.067	0.003	2.24	0.09
1173	0.149	0.003	4.7	0.1	0.060	0.001	2.00	0.04
1274	0.14	0.01	5.0	0.4	0.056	0.004	1.88	0.13
1333	0.141	0.003	4.92	0.11	0.057	0.001	1.89	0.04
1408	0.12	0.01	5.78	0.48	0.048	0.004	1.61	0.13

Table 7C
 γ radiation shielding parameters of concrete C after annealing at 400 °C.

SAMPLE C								
Energy/keV	μ /cm ⁻¹	$\Delta\mu$ /cm ⁻¹	I_{HVL} /cm	I_{HVL} /cm	μ_m /cm ⁻¹	μ_m /cm ⁻¹	σ_a /b/atom	$\Delta\sigma_a$ /b/atom
122	0.411	0.032	1.69	0.13	0.162	0.013	5.22	0.41
245	0.36	0.01	1.925	0.053	0.142	0.004	4.57	0.13
344	0.288	0.003	2.407	0.025	0.113	0.001	3.66	0.04
511	0.219	0.004	3.165	0.058	0.086	0.002	2.78	0.05
662	0.20	0.01	3.47	0.18	0.079	0.004	2.54	0.13
779	0.184	0.016	3.77	0.33	0.072	0.006	2.34	0.20
964	0.163	0.015	4.25	0.40	0.064	0.006	2.07	0.19
1086	0.162	0.011	4.28	0.30	0.064	0.004	2.06	0.14
1112	0.158	0.009	4.39	0.25	0.062	0.004	2.01	0.11
1173	0.153	0.008	4.53	0.24	0.060	0.003	1.94	0.10
1274	0.144	0.005	4.81	0.17	0.057	0.002	1.83	0.06
1333	0.146	0.008	4.75	0.26	0.057	0.003	1.85	0.10
1408	0.150	0.017	4.62	0.53	0.059	0.007	1.90	0.22

curing temperature of 25 °C. In the evaluation of mechanical performances, the evaluated results of cold crushing strength of the C-A, C-B, and C-C concretes, exhibited a negligible decrease in CCS values for all samples heat treated between 110 and 400 °C. The CCS for samples heat-treated at 200 °C decreased by 13, 10, and 9 % of the initial value for the concretes C-A, C-B, and C-C dried at 110 °C, respectively. The concretes C-A, C-B, and C-C heat-treated at 400 °C had a decreasing CCS by 16, 16 and 13 % of the initial value for samples dried at 110 °C. Going into details, the C-C concrete attained the best CCS values above 90 MPa versus heat treatment temperatures, whereas the C-A concrete exhibits

the CCS above 80 MPa. The C-B concrete had the lowest compressive strength varied in the range of ca. 50–60 MPa. Nevertheless, the compressive strength of all mixtures after casting (25 °C) and drying (110, 200 and 400 °C) satisfies the requirements of shielding refractory concretes. It was also found that the hydrated matrix of concretes tends to decompose below ca. 350 °C but the strength of the concretes was affected slightly.

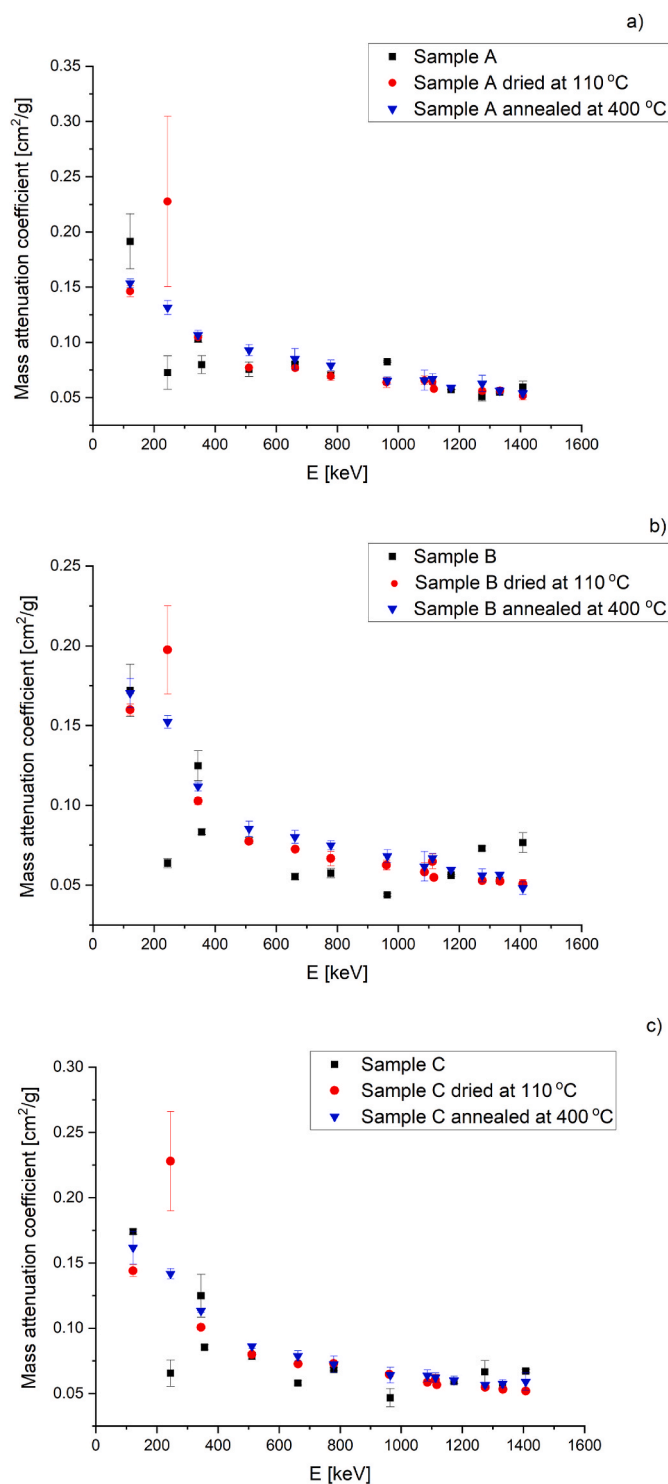


Fig. 19. Distributions of the estimated mass attenuation coefficients for concrete A, B and C obtained before and after water removal.

3.3.3. Determination of the γ quanta attenuation properties of the studied concretes

As described in Sec. 2.4 we have determined the linear attenuation coefficients of the three studied concretes, μ , for γ -rays in the range of 81–1408 keV. The measured dependencies of the γ -lines intensities as a function of the concretes thickness were fitted in both, the exponential and logarithmic form. This allowed the determination of the systematic uncertainties due to the assumed model. The measurements and data analysis were done for the three studied concretes after drying at 110 °C,

annealing at 400 °C, and before these procedures. The obtained values of μ and Half-Value Layer (L_{HVL}), and total atomic cross section (σ_a) are shown for all the studied materials in Table 5A–C.

Analogous results for the same samples of concretes after drying at 110 °C and annealing at 400 °C are gathered in Table 6A–C and Table 7A–C, respectively. The results before and after water removal are compared in Fig. 19.

In general, the two materials enriched in Ba and Fe (samples B and C, respectively) exhibit better shielding properties than the material A. However, due to the relatively small content of these higher atomic number elements, the increase of the attenuation coefficients is quite weak and well pronounced only for the higher γ -rays energies (~1200–1400 keV). In the energy range up to 500 keV the results suggest, that the presence of Ba and Fe and the increased density of materials B and C are not relevant. However, any conclusions in this energy range should be drawn with caution due to the complex energy spectrum of ^{152}Eu and the associated systematic uncertainties in the analysis performed. The same applies to the effect of drying and annealing which can be clearly seen only for concrete B. In this case, the removal of water seems to increase the shielding properties in the energies range of about 500–1000 keV, while the tendency changes at the highest energies studied. This effect may be explained only by the fact, that the elevated temperature affects not only the water content of the material but also its porosity. This can be seen by looking at the density change of sample B which did not follow exactly the mass loss. These conclusions should, however, be treated with some caution due to the short exposure to the higher temperatures compared to the operating conditions in the nuclear reactor.

4. Conclusions

This study comprehensively assessed the γ radiation shielding properties of bauxite-based concrete using experimental and theoretical approaches within the energy range of 81–1408 keV. The Concrete design used fixed contents of both bauxite aggregate and cement, as well as a constant water/cement ratio. In all three concrete types, three types of cement were used, commercial calcium aluminate cement (C-A), Ba-doped C-A-Z as-synthesized cement (C-B) and Fe-doped as-synthesized cement C-A-Z (C-C). The prepared as-synthesized cement and its hydration behavior were characterized using XRD, SEM-EDS, and DSC-TG-EGA(MS). The prepared concretes were characterized using XRD, SEM-EDS, compressive strength, density, and gamma radiation shielding. The following observations have been obtained:

- 1) The XRD patterns of the synthesized cements prove a type of multi-phased binder.
- 2) The doping BaO and Fe₂O₃ components were chemically bonded within the hydrated cement matrix. The hydrates of the CaO-BaO-Al₂O₃-H₂O and CaO-Al₂O₃-Fe₂O₃-H₂O-type were formed. These hydrates are thermally stable up to ca. 110 °C.
- 3) The maximum weight loss of concretes was found at 110 °C, and was associated mainly with the evaporation of the capillary water and the physically adsorbed water (gel water). The chemically bound water (crystal water) occurring in hydrates was released at higher temperatures below i.e. 400 °C, as it was confirmed by DSC-TG-EGA (MS).
- 4) This resulted in slight variations of the volumetric density of the concretes.
- 5) The microscopic studies utilized the SEM to examine the microstructure and morphology of the cement pastes and the concretes. A strong connection between bauxite aggregates and a fine-grained matrix of concretes was shown.
- 6) γ -ray attenuation studies using ^{22}Na , ^{137}Cs , ^{60}Co , ^{133}Ba and ^{152}Eu sources showed that the shielding of the studied concretes was improved as compared with ordinary concrete presented in the National Institute of Standards and Technology (NIST) database [90].

The obtained attenuation parameters are, however, smaller than in our previous studies [20].

- 7) The effect of elevated temperature does not affect significantly the γ radiation attenuation properties of the studied bauxite-based refractory concrete which suggests that they may be very useful as shielding materials in severe thermal working conditions, e.g. in nuclear reactors.

CRedit authorship contribution statement

Dominika Madej (65%): Conceptualization, Methodology, Software, Validation, Formal analysis, Investigation, Resources, Data curation, Visualization, Funding acquisition, Project administration, Supervision, Writing - original draft, Writing - review & editing; Michał Silarski (25%): Investigation, Methodology, Validation, Funding acquisition, Writing - original draft; Palina Cherkes (10%): Investigation.

Declaration of competing interest

The authors declare that they have no known competing financial interests or personal relationships that could have appeared to influence the work reported in this paper.

Data availability

No data was used for the research described in the article.

Acknowledgements

This project was financed by the National Science Centre, Poland, project number 2017/26/D/ST8/00012 (Recipient: D. Madej). This work was also partly supported by the statutory funds of the Faculty of Material Science and Ceramics AGH University of Krakow, Poland with the Agreement no. 16.16.160.557.

The SEM-EDS investigations were supported by the program "Excellence Initiative - Research University" for the AGH University of Krakow, grant ID 1449.

We acknowledge support by the EU Horizon 2020 Research and Innovation Programme under the Marie Skłodowska-Curie Grant Agreement No. 101006726, and grants U1U/P06/NW/02.07 and U1U/P07/NO/17.13 from the DigiWorld and Anthropocene Priority Research Areas under the Strategic Programme Excellence Initiative at the Jagiellonian University (Recipient: M. Silarski, P. Cherkes).

References

- B. Kanagaraj, N. Anand, A.D. Andrushia, M.Z. Naser, Recent developments of radiation shielding concrete in nuclear and radioactive waste storage facilities – a state of the art review, *Construct. Build. Mater.* 404 (2023) 133260.
- M.-S. Yim, H. Ocken, Radiation dose management in nuclear power plants, *Prog. Nucl. Energy* 39 (1) (2001) 31–51.
- İ.B. Topçu, Properties of heavyweight concrete produced with barite, *Cement Concr. Res.* 33 (6) (2003) 815–822.
- D. Rezaei-Ochbelagh, S. Azimkhani, Investigation of gamma-ray shielding properties of concrete containing different percentages of lead, *Appl. Radiat. Isot.* 70 (10) (2012) 2282–2286.
- A.T. Şensoy, H.S. Gökçe, Simulation and optimization of gamma-ray linear attenuation coefficients of barite concrete shields, *Construct. Build. Mater.* 253 (2020) 119218.
- J.M. Danforth, D.D. Pearson, A.A. Goodarzi, *Ionizing Radiation Toxicology*, Encyclopedia of Toxicology, fourth ed., 5, 2024, pp. 629–653.
- C. Busby, Ionizing radiation and cancer: the failure of the risk model, *Cancer Treatment and Research Communications* 31 (2022) 100565.
- H.C. Manjunatha, L. Seenappa, B.M. Chandrika, C. Hanumantharayappa, A study of photon interaction parameters in barium compounds, *Ann. Nucl. Energy* 109 (2017) 310–317.
- C.V. Vishnu, A. Joseph, Gamma-ray shielding analysis on natural rubber composites fortified with barium tungstate (BaWO₄), *Radiat. Phys. Chem.* 216 (2024) 111389.
- R. Umashankara Raja, H.C. Manjunatha, Y.S. Vidya, R. Munirathnam, K.N. Sridhar, K.M. Rajashekara, S. Manjunatha, Effect of chromium substitution on the gamma and neutron radiation shielding properties of calcium hexaferrite nanoparticles, *Appl. Phys. A* 129 (2023) 709.
- M.E.M. Eisa, M.D.M. Ali, M.J. Abuualreish, Study of gamma-ray shielding of two different heavy metals and their combination for Cs-137 and Co-60 sources, *Eng. Technol. Appl. Sci. Res.* 13 (1) (2023) 10033–10038.
- A. Abdel-latif M, M.M. Kassab, Effect of chromium contents on radiation shielding and macroscopic cross-section in steel alloys, *Appl. Radiat. Isot.* 186 (2022) 110263.
- Anti-X, Gamma Ray and Neutron Radiation Shielding Material and Preparation Method Thereof, CN106566013A.
- B.M. Chandrika, Holaly Chandrashekara Shastry Manjunatha, K.N. Sridhar, M. R. Ambika, L. Seenappa, S. Manjunatha, R. Munirathnam, A.J. Clement Lourduraj, Synthesis, physical, optical and radiation shielding properties of barium-bismuth oxide borate-A novel nanomaterial, *Nucl. Eng. Technol.* 55 (5) (2023) 1783–1790.
- M.I. Sayyed, G. Lakshminarayana, M.G. Dong, M. Çelikbilek Ersundu, A. E. Ersundu, I.V. Kityk, Investigation on gamma and neutron radiation shielding parameters for BaO/SrO-Bi₂O₃-B₂O₃ glasses, *Radiat. Phys. Chem.* 145 (2018) 26–33.
- M.S. Al-Buriah, C. Eke, S. Alomairy, C. Mutuwong, N. Sfina, Micro-hardness and gamma-ray attenuation properties of lead iron phosphate glasses, *J. Mater. Sci. Mater. Electron.* 32 (2021) 13906–13916.
- Y. Yao, X. Zhang, M. Li, R. Yang, T. Jiang, J. Lv, Investigation of gamma ray shielding efficiency and mechanical performances of concrete shields containing bismuth oxide as an environmentally friendly additive, *Radiat. Phys. Chem.* 127 (2016) 188–193.
- M.M. Hivrekar, D.B. Sable, M.B. Solunke, K.M. Jadhav, Network structure analysis of modifier CdO doped sodium borate glass using FTIR and Raman spectroscopy, *J. Non-Cryst. Solids* 474 (2017) 58–65.
- Y.A. Abdelghany, M.M. Kassab, M.M. Radwan, M.A. Abdel-Latif, Borotellurite glass system doped with ZrO₂, potential use for radiation shielding, *Prog. Nucl. Energy* 149 (2022) 104256.
- D. Madej, M. Silarski, S. Parzych, Design, structure, microstructure and gamma radiation shielding properties of refractory concrete materials containing Ba- and Sr-doped cements, *Mater. Chem. Phys.* 260 (2021) 124095.
- A. Zezulová, T. Staněk, T. Opravil, The influence of barium sulphate and barium carbonate on the portland cement, *Procedia Eng.* 151 (2016) 42–49.
- N.J. Abualroos, K.A. Yaacob, R. Zainon, Radiation attenuation effectiveness of polymer-based radiation shielding materials for gamma radiation, *Radiat. Phys. Chem.* 212 (2023) 111070.
- L. Seenappa, H.C. Manjunatha, B.M. Chandrika, Hanumantharayappa Chikka, A study of shielding properties of X-ray and gamma in barium compounds, *Journal of Radiation Protection and Research* 42 (1) (2017) 26–32.
- K.V. Sathish, H.C. Manjunatha, Y.S. Vidya, K.N. Sridhar, L. Seenappa, B. Chinnappa Reddy, S. Alfred Cecil Raj, P.S. Damodara Gupta, X-rays/gamma rays radiation shielding properties of barium-nickel-iron oxide nanocomposite synthesized via low temperature solution combustion method, *Radiat. Phys. Chem.* 194 (2022) 110053.
- S.-C. Kim, K.-R. Dong, W.-K. Chung, Medical radiation shielding effect by composition of barium compounds, *Ann. Nucl. Energy* 47 (2012) 1–5.
- A.S. Abouhaswa, F.I. El-Agawany, Emad M. Ahmed, Y.S. Rammah, Optical, magnetic characteristics, and nuclear radiation shielding capacity of newly synthesized barium boro-vanadate glasses: B₂O₃-BaF₂-Na₂O-V₂O₅, *Radiat. Phys. Chem.* 192 (2022) 109922.
- R. Polat, Z. Yalçın, O. İçelli, The absorption jump factor of effective atomic number and electronic density for some barium compounds, *Nucl. Instrum. Methods Phys. Res. Sect. A Accel. Spectrom. Detect. Assoc. Equip.* 629 (1) (2011) 185–191.
- Z. Ding, S.Q. Shi, H. Zhang, L. Cai, Electromagnetic shielding properties of iron oxide impregnated kenaf bast fiberboard, *Compos. B Eng.* 78 (2015) 266–271.
- O. Gencil, A. Bozkurt, E. Kam, T. Korkut, Determination and calculation of gamma and neutron shielding characteristics of concretes containing different hematite proportions, *Ann. Nucl. Energy* 38 (12) (2011) 2719–2723.
- K. Gunoglu, İ. Akkurt, Radiation shielding properties of concrete containing magnetite, *Prog. Nucl. Energy* 137 (2021) 103776.
- B. Oto, A. Gür, E. Kavaz, T. Çakır, N. Yaltay, Determination of gamma and fast neutron shielding parameters of magnetite concretes, *Prog. Nucl. Energy* 92 (2016) 71–80.
- R. Florez, H.A. Colorado, A. Alajo, C.H.C. Giraldo, The material characterization and gamma attenuation properties of Portland cement-Fe₃O₄ composites for potential dry cask applications, *Prog. Nucl. Energy* 111 (2019) 65–73.
- C. Thomas, J. Rico, P. Tamayo, J. Setién, F. Ballester, J.A. Polanco, Neutron shielding concrete incorporating BaC and PVA fibers exposed to high temperatures, *J. Build. Eng.* 26 (2019) 100859.
- İ. Erkoynucu, İ. Demirkol, F. Akman, K. Dilsiz, M.R. Kaçal, H. Polat, A detailed investigation of gamma and neutron shielding capabilities of concrete doped with bronze and boron carbide, *Radiat. Phys. Chem.* 215 (2024) 111358.
- Mohamed Amin, W.E. Elemam, M.A. Kandil, M. Samy, Effect of heavy-weight recycled materials on radiation shielding and properties of high-strength concrete with CEM III, *J. Build. Eng.* 79 (2023) 107819.
- U. Chandru, A. Bahurudeen, R. Senthilkumar, Systematic comparison of different recycled fine aggregates from construction and demolition wastes in OPC concrete and PPC concrete, *J. Build. Eng.* 75 (2023) 106768.
- T. Shams, M. Eftekhar, A. Shirani, Investigation of gamma radiation attenuation in heavy concrete shields containing hematite and barite aggregates in multi-layered and mixed forms, *Construct. Build. Mater.* 182 (2018) 35–42.
- A.S. Ouda, Development of high-performance heavy density concrete using different aggregates for gamma-ray shielding, *Prog. Nucl. Energy* 79 (2015) 48–55.

- [39] Q. Wang, Y. Wang, B. Zhou, L. Wang, Y. Fang, S. Xu, Influence of polypropylene fibers on the mechanical properties of radiation shielding concrete with barite aggregates, *J. Build. Eng.* 79 (2023) 107820.
- [40] M. Dąbrowski, D. Jozwiak-Niedzwiedzka, K. Bogusz, M.A. Glinicki, Influence of serpentinite aggregate on the microstructure and durability of radiation shielding concrete, *Construct. Build. Mater.* 337 (2022) 127536.
- [41] S. K k, M.S. T retken, N.  ks zer, H.S. G k e, Effect of elevated temperature on radiation shielding properties of cement and geopolymer mortars including barite aggregate and colemanite powder, *Materialia* 27 (2023) 101693.
- [42] P. Prochon, T. Piotrowski, The effect of cement and aggregate type and w/c ratio on the bound water content and neutron shielding efficiency of concretes, *Construct. Build. Mater.* 264 (2020) 120210.
- [43] S.I.A. Ali, E. Lubl y, Effect of elevated temperature on the magnetite and quartz concrete at different W/C ratios as nuclear shielding concretes, *Nuclear Materials and Energy* 33 (2022) 101234.
- [44] A.U. Rehman, M. Atif, S. Baqi, A. Ul-Hamid, U. ur Rehman, W. Khalid, Z. Ali, F.C.-C. Ling, M. Nadeem, Enhancement in the electromagnetic shielding properties of doped $M_{0.01}Fe_{2.99}O_4$ magnetite nanoparticles ($M = Mn^{2+}, Ni^{2+}, Cu^{2+}, Zn^{2+}$), *J. Alloys Compd.* 960 (2023) 171051.
- [45] O. Gencel, W. Brostow, C. Ozel, M. Filiz, Concretes containing hematite for use as shielding barriers, *Mater. Sci.* 16 (3) (2010) 249–256.
- [46] M. Safamehr, M. Izadnia, S.H. Hashemi, S. Koohestani, Nanosilica role in concrete containing iron oxides aggregates and boron carbide as a shield against gamma rays, *Cement-Wapno-Beton = Cement Lime Concrete* 26 (3) (2021) 218–232.
- [47] O. Gencel, Effect of elevated temperatures on mechanical properties of high-strength concrete containing varying proportions of hematite, *Fire Mater.* 36 (2012) 217–230.
- [48] W.H. Abulfaraj, S.M. Kamal, Evaluation of ilmenite serpentine concrete and ordinary concrete as nuclear reactor shielding, *Radiat. Phys. Chem.* 44 (1–2) (1994) 139–148.
- [49] A.M.I. Kany, M.I. El-Gohary, S.M. Kamal, Thermal, epithermal and thermalized neutron attenuation properties of ilmenite-serpentine heat resistant concrete shield, *Radiat. Phys. Chem.* 44 (1–2) (1994) 157–160.
- [50] A.S. Makarios, F.M. Sayedahmed, Radial attenuation of thermal neutrons around a joint in a straight duct in an ilmenite concrete shield, *International Journal of Radiation Applications and Instrumentation. Part A, Appl. Radiat. Isot.* 40 (6) (1989) 473–476.
- [51] I.I. Bashter, Radiation attenuation and nuclear properties of high density concrete made with steel aggregates, *Radiat. Eff. Defect Solid* 140 (3–4) (1997) 351–364.
- [52] I.I. Bashter, A.S. Makarios, A.E.-S. Abdo, Investigation of hematite-serpentine and ilmenite-limonite concretes for reactor radiation shielding, *Ann. Nucl. Energy* 23 (1) (1996) 65–71.
- [53] M. Lardhi, F. Mukhtar, Radiation shielding performance of seawater-mixed concrete incorporating recycled coarse aggregate and steel slag, *Journal of Radiation Research and Applied Sciences* 16 (1) (2023) 100528.
- [54] A.M. Ibrahim, A.R. Mohamed, A.M. El-Khatib, M.T. Alabsy, M. Elsalamawy, Effect of hematite and iron slag as aggregate replacement on thermal, mechanical, and gamma-radiation shielding properties of concrete, *Construct. Build. Mater.* 310 (2021) 125225.
- [55] Y.S. Choi, S.M. Lee, Fundamental properties and radioactivity shielding performance of concrete recycled cathode ray tube waste glasses and electric arc furnace slag as aggregates, *Prog. Nucl. Energy* 133 (2021) 103649.
- [56] R. Farokhzad, A. Dadashi, A. Sohrabi, The effect of ferrophosphorus aggregate on physical and mechanical properties of heavy-weight concrete, *Construct. Build. Mater.* 299 (2021) 123915.
- [57] M.H. Kharita, S. Yousef, M. AlNassar, Review on the addition of boron compounds to radiation shielding concrete, *Prog. Nucl. Energy* 53 (2) (2011) 207–211.
- [58] M.B. Stone, A.I. Kolesnikov, V.R. Fanelli, A.F. May, Shuang Bai, J. Liu, Characterization of aluminum and boron carbide based additive manufactured material for thermal neutron shielding, *Mater. Des.* 237 (2024) 112463.
- [59] C. Zhu, G. Li, J. Wang, S. Dong, K. Cao, Y. Lv, Performance improvement in neutron-shielding ultra-high performance mortar prepared with alkaline-treated boron carbide, *J. Build. Eng.* 71 (2023) 106435.
- [60] Y. Zhang, J. Wang, L. Zhang, C. Li, H. Jiang, X. Ba, D. Hou, Study on the preparation and properties of high-belite cementitious materials from shield slag and calcium carbide slag, *Construct. Build. Mater.* 355 (2022) 129082.
- [61] B. Bayrak, A.  z, A. Benli, E. Kavaz, G. Kaplan, A.C. Aydın, Physico-mechanical and shielding properties of alkali-activated slag composites incorporating cement clinker aggregate: effect of high temperature and particle size, *J. Build. Eng.* 67 (2023) 105982.
- [62] B. Han, L. Zhang, J. Ou, Smart and Multifunctional Concrete toward Sustainable Infrastructures, Springer Singapore, 2017.
- [63] O. Kilicoglu, Chaitali V. More, U. Kara, Metin Davraz, Investigation of the effect of cement type on nuclear shield performance of heavy concrete, *Radiat. Phys. Chem.* 209 (2023) 110954.
- [64] L. Luo, Z. Chen, Q. Tao, L. Xie, D. Jin, Z. Li, D. Deng, Effects of high temperatures on the splitting tensile strength and gamma ray shielding performance of radiation shielding concrete, *Construct. Build. Mater.* 343 (2022) 127953.
- [65] L. Luo, Z. Chen, S. Cai, Q. Tao, L. Xie, D. Jin, Mechanics, γ -ray shielding properties and acoustic emission characteristics of radiation shielding concrete exposed to elevated temperatures, *Case Stud. Constr. Mater.* 19 (2023) e02572.
- [66] I.M. Nikbin, A. Rafiee, S. Dezhampannah, S. Mehdipour, R. Mohebbi, H. H. Moghadam, A. Sadrmomtazi, Effect of high temperature on the radiation shielding properties of cementitious composites containing nano-Bi $_2$ O $_3$, *J. Mater. Res. Technol.* 9 (5) (2020) 11135–11153.
- [67] E. Sancak, Y.D. Sari, O. Simsek, Effects of elevated temperature on compressive strength and weight loss of the light-weight concrete with silica fume and superplasticizer, *Cement Concr. Compos.* 30 (8) (2008) 715–721.
- [68] D. Madej, A. Kruk, Tracing the early and long-term hydration of fast setting cementitious material (Ca $_7$ ZrAl $_6$ O $_{18}$) and calcium aluminate cement (CAC) pastes by means of electrochemical impedance spectroscopy and other methods, *Construct. Build. Mater.* 164 (2018) 94–102.
- [69] A. Kruk, D. Madej, A new approach to time-resolved electrochemical impedance spectroscopy using the Impedance Camera to track fast hydration processes in cement-based materials, *Measurement* 205 (2022) 112199.
- [70] D. Madej, R. Boris, Synthesis, characterization and hydration analysis of Ba $^{2+}$, Cu $^{2+}$ or Bi $^{3+}$ -doped CaO-Al $_2$ O $_3$ -ZrO $_2$ -based cements, *J. Therm. Anal. Calorim.* 138 (2019) 4331–4340.
- [71] M. Kurudirek, M. Aygun, S.Z. Erzeno lu, Chemical composition, effective atomic number and electron density study of trommel sieve waste (TSW), Portland cement, lime, pointing and their admixtures with TSW in different proportions *Appl. Radiat. Isotopes* 68 (2010) 1006–1011.
- [72] E. Litwinek, D. Madej, Structure, microstructure and thermal stability characterizations of C $_3$ AH $_6$ synthesized from different precursors through hydration, *J. Therm. Anal. Calorim.* 139 (2020) 1693–1706.
- [73] D. Madej, J. Szczerba, W. Nocu n-Wczelik, R. Gajerski, Hydration of Ca $_7$ ZrAl $_6$ O $_{18}$ phase, *Ceram. Int.* 38 (5) (2012) 3821–3827.
- [74] D. Madej, J. Szczerba, K. Dul, Phase transformation during the decomposition of hydrated calcium zirconium aluminate (Ca $_7$ ZrAl $_6$ O $_{18}$) paste subjected to various dehydration temperatures, *Thermochim. Acta* 597 (2014) 27–34.
- [75] D. Madej, A. Kruk, Monitoring hydration of Sr-doped calcium zirconium aluminate (Ca,Sr) $_7$ ZrAl $_6$ O $_{18}$ cement via electrochemical impedance spectroscopy (EIS) and supported techniques, *Construct. Build. Mater.* 206 (2019) 307–320.
- [76] D. Madej, Synthesis and hydraulic activity of novel Sr $^{2+}$ -doped Ca $_7$ ZrAl $_6$ O $_{18}$ cement at 50 C, *Thermochim. Acta* 661 (2018) 98–105.
- [77] A. Nawaz, N. Kim, J. Seo, S.Z. Farooq, H.K. Lee, Hydration and phase conversion of MgO-modified calcium aluminate cement, *Construct. Build. Mater.* 369 (2023) 130425.
- [78] R. Risoluti, D. Piazzese, A. Napoli, S. Materazzi, Study of [2-(2-pyridyl)imidazole] complexes to confirm two main characteristic thermoanalytical behaviors of transition metal complexes based on imidazole derivatives, *J. Anal. Appl. Pyrol.* 117 (2016) 82–87.
- [79] M. Kosi nska-Pezda, L. Zapala, U. Maciolek,  . Byczy nski, E. Wo znicka, W. Zapala, Thermal study, temperature diffraction patterns and evolved gas analysis during pyrolysis and oxidative decomposition of novel ternary complexes of light lanthanides with mafenamic acid and 1,10-phenanthroline, *J. Anal. Appl. Pyrol.* 159 (2021) 105293.
- [80] Г.Ю. Флейшер, В.В. Токарчук, В.А. Свѣрський, The effect of nitrogen-containing organic admixtures on the chemical processes of cement hardening, *E. Eur. J. Enterprise Technol.* 1 (6) (2016) 46–54, 79.
- [81] R.L. Hill, The Study of Hydration of Fly Ash in the Presence of Calcium Nitrate and Calcium Formate, Doctoral dissertation, (unpublished research work), Texas, 1994.
- [82] R. Hill, K. Daugherty, The interaction of calcium nitrate and a Class C fly ash during hydration, *Cement Concr. Res.* 26 (7) (1996) 1131–1143.
- [83] S.M. Bushnell-Watson, J.H. Sharp, The detection of the carboaluminate phase in hydrated high alumina cements by differential thermal analysis, *Thermochim. Acta* 93 (1985) 613–616.
- [84] D. Madej, Hydration, carbonation and thermal stability of hydrates in Ca $_7$ -xSr $_x$ ZrAl $_6$ O $_{18}$ cement, *J. Therm. Anal. Calorim.* 131 (2018) 2411–2420.
- [85] J. Bensted, P. Barnes (Eds.), Structure and Performance of Cements, second ed., CRC Press, 2014, pp. 122–123.
- [86] C. Phrompet, C. Sriwong, C. Ruttanapun, Mechanical, dielectric, thermal and antibacterial properties of reduced graphene oxide (rGO)-nanosized C $_3$ AH $_6$ cement nanocomposites for smart cement-based materials, *Compos. B Eng.* 175 (2019) 107128.
- [87] C.M. George, Industrial aluminate cements, in: P. Barnes (Ed.), Structure and Performance of Cements, Applied Science Publishers, London, 1983, pp. 415–470.
- [88] N. Ukrainczyk, T. Matusinovic, S. Kurajica, B. Zimmermann, J. Sipusic, Dehydration of a layered double hydroxide-C $_2$ AH $_8$, *Thermochim. Acta* 464 (1–2) (2007) 7–15.
- [89] BSI. BS 8500-1: 2002, Concrete-complementary British Standard to BS EN 206-1-Part 1: Method of Specifying and Guidance for the Specifier, 2002.
- [90] J.H. Hubbell  and S. M. Seltzer, Tables of X-ray mass attenuation coefficients and mass energy-absorption coefficients from 1 keV to 20 MeV for elements Z = 1 to 92 and 48 additional substances of dosimetric Interest, Radiation Physics division, PML, NIST (DOI: <https://dx.doi.org/10.18434/T4D01F>).